

A DIGITAL KINETICS PARADIGM FOR THE
MESO-SCALE MODELING OF MICROSTRUCTURAL
EVOLUTION IN THE PRESENCE OF A DIFFUSING
SOLUTE

BY

BRADLEY R. CRUME

ProQuest Number: 10794766

All rights reserved

INFORMATION TO ALL USERS

The quality of this reproduction is dependent upon the quality of the copy submitted.

In the unlikely event that the author did not send a complete manuscript and there are missing pages, these will be noted. Also, if material had to be removed, a note will indicate the deletion.



ProQuest 10794766

Published by ProQuest LLC (2018). Copyright of the Dissertation is held by the Author.

All rights reserved.

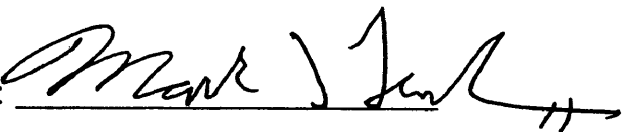
This work is protected against unauthorized copying under Title 17, United States Code
Microform Edition © ProQuest LLC.

ProQuest LLC.
789 East Eisenhower Parkway
P.O. Box 1346
Ann Arbor, MI 48106 – 1346

A thesis submitted to the Faculty and Board of Trustees of the Colorado School of Mines in partial fulfillment of the requirements for the degree of Master of Science (Engineering Systems).

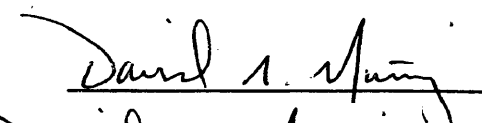
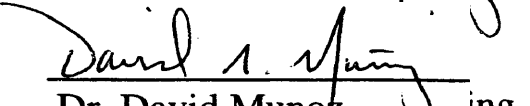
Golden, Colorado
Date Jan 21, 2004

Signed: 
Bradley Crume

Approved: 

Dr. Mark Lusk
Thesis Advisor

Golden, Colorado
Date 1/21/04



Dr. David Munoz ing

ABSTRACT

This thesis introduces a discrete, probabilistic paradigm for the simulation of precipitation and grain growth at the meso-scale. This digital kinetics scheme, based on Monte Carlo simulations is meant to complement existing phase-field and sharp-interface modeling methods. The digital kinetics approach employs probabilistic, discrete event simulations for both the solute migration and migration of phase boundaries. Parameters from the digital kinetics model can be linked to the phase-field model which, is in turn, linked to the sharp interface model via asymptotic analyses. Results are presented which indicate that the new paradigm delivers the correct qualitative features for both precipitation and grain growth. Some preliminary validation of the model is also provided.

CONTENTS

ABSTRACT	iii
LIST OF FIGURES	xi
ACKNOWLEDGMENTS	xii
1 INTRODUCTION	1
2 BACKGROUND	7
2.1 Diffusion	7
2.2 Microstructural Evolution	11
2.2.1 Precipitation and Coarsening	12
2.2.2 Driving Forces of Boundary Migration	15
2.2.3 Einstein Relation for Migration	18
2.3 Experimental and Theoretical Studies of Grain Boundaries	20
2.4 Numerical Modeling of Grain Boundary Motion	26
2.4.1 Phase-field: Continuum-theory approach	27
2.4.2 Discrete Models	33

2.4.2.1	Molecular Dynamics Diffusion	34
2.4.2.2	Ising/Potts Approach to Phase Evolution	36
3	SHARP-INTERFACE MODEL	41
3.0.3	Precipitation	45
3.0.3.1	Non-dimensional Form of Equations	46
3.0.3.2	Equilibrium Area	48
3.0.4	Grain Coarsening	49
3.0.4.1	Non-dimensional Form of Equations	49
3.0.4.2	Implementation	52
4	PHASE-FIELD MODEL	53
4.0.5	Non-dimensionalization - General System	56
4.0.6	Non-dimensionalization - Grain Coarsening	59
4.0.7	Non-dimensionalization - Precipitation	61
4.1	Numerical Implementation of the Phase-Field Model	62
4.1.1	Finite Difference Approximation	62
4.1.2	Gauss-Seidel Algorithm	64
5	DIGITAL KINETICS MODEL	68

5.1	Digital Kinetics Diffusion	70
5.1.1	Grain Boundary Effects on Diffusion	74
5.2	Microstructural Evolution	76
6	RESULTS	80
6.1	Diffusion Check	81
6.2	Precipitation	82
6.3	Grain Coarsening	91
7	DISCUSSION	95
7.1	Diffusion	96
7.2	Precipitation	97
7.3	Grain Coarsening	100
7.4	Further Research	100
7.5	Conclusions	102
APPENDICES		
A.	Appendix: Asymptotic Analysis of the GL Model	111
	Precipitation	113
	Outer expansion	113

Inner Expansion	114
Grain Coarsening	117
Outer expansion	117
Inner Expansion	118
B. Appendix: Parabolic Approximation of Free Energy Curve	121

LIST OF FIGURES

1.1	Examples of cross-sectional solute concentration profiles resulting from simulations based on the digital kinetics, phase-field and sharp-interface models, respectively:	5
2.1	Free energy curves for phases α and β in a binary solution of components A and B.	11
2.2	Solute drag effect on the relationship between interface velocity and driving force.	21
2.3	The concentration profile across a grain boundary as determined from the phase-field model created by Cha et.al.[39]. The distance is scaled with sample thickness λ	30
2.4	Results of Ising-model phase evolution/atomistic diffusion showing solute drag effects of impurities from Mendeleev and Srolovitz[48]. Symbols are model results, x's are results for no impurities, other symbols for increasing impurity concentration. Dashed lines are predictions from Cahn-Lücke-Stüwe analytical model.	39

2.5	The system of interstitial solute atoms (circles) and lattice sites (crosses) used by Mendeleev and Srolovitz for Potts model simulations.	40
4.1	Cross sectional view of the axisymmetric system and configuration of phase-field parameters.	57
4.2	Relaxation of phase-field from sharp-interface initial condition after 10 pseudo-time steps. There is no driving force on the boundary ($\rho_i = 1$, $\epsilon = 0.1$, $\Delta x = 0.02$).	67
6.1	Concentration profile solutions to diffusion in 2-D lattice. The lighter line is the phase-field solution, darker, uneven line is the digital kinetics solution.	83
6.2	Examples of digital kinetics simulations with unstable parameters. Left: $\Delta\rho = 0.005$, $M_{DK} = 5.0$; Right: $\Delta\rho = 0.01$, $M_{DK} = 0.005$	84
6.3	Solution to the evolution of the fractional precipitate area from the phase-field model. The straight line shown is at the sharp-interface prediction of 0.193.	85
6.4	Concentration profiles for phase-field precipitation modeling results at various time steps.	86

6.5 Solution to the evolution of the equilibrium precipitate area from the digital kinetics model. The straight line indicates averaged equilibrium precipitate size. 87

6.6 Concentration profiles for digital kinetics precipitation modeling results at various time steps. 88

6.7 Precipitate area fraction solution from four trials of the digital kinetics code using the same parameters but different initial seed. 89

6.8 Each of the plots represents four trails of the digital kinetics code with different random number generator seeds. 90

6.9 Results of coarsening runs in the sharp-interface and phase-field models for different values of K_n 92

6.10 Comparison of sharp-interface results (dashed) with phase-field runs using decreasing boundary width. 1000 grid points used for $\varepsilon = 0.10, 0.05$; 4000 grid points used for $\varepsilon = 0.025$ 93

6.11 Cross sectional profile of grain growth solutions. The dash-dotted line is phase-field solution while the solid line is the digital kinetics. The time scale comes from the phase-field model. 94

7.1 Comparison of Gibbs free energy of the form of eqn. B.36, a parabolic function fit to eqn B.36 and the error associated with the fit function. 123

ACKNOWLEDGMENTS

I would like to express my gratitude to my advisor Professor Mark Lusk. This research is based on work begun by him and further developed by Herng-Jeng Jou. Extraordinary work was done by Phillip Liu on a similar model; whatever impact this research has will be due in no small part to his diligence. The thesis would not have been possible without the contributions of each of these peers, though the greatest contribution is friendship that Mark has shown me.

I greatly appreciate the review and time spent by my committee members-Dr. Garth Jensen (ITN Energy Systems), Profs. Terry Parker and David Wood.

Mike Seman (Colorado School of Mines) deserves accolades for his heroic efforts in assisting with the abandoned experimental efforts of this research. Dr. Elizabeth Holm (Sandia National Laboratories) provided some valuable insights and leads that helped focus my research. Maureen Wan and my family provided constant moral support. Finally I would like to thank Taeko Enomoto for the sacrifice she made over the last year. She is the motivation for finishing my degree.

CHAPTER 1

INTRODUCTION

An understanding of the evolution of material microstructure is central to most engineering applications. Continuing trends of producing components with ever tighter tolerances and increasingly exotic combinations of materials suggest that efforts to understand such microstructural evolution will play a prominent role for the foreseeable future. Thin film sciences, ceramics, and cutting edge metallurgy applications all rely on the ability to control the evolution of a material through diffusional and structural transformations to produce materials with predictable properties. The external controls employed in production techniques often affect multifaceted system reactions.

The meso-scale modeling of solute diffusion away from interfaces can be modeled using continuum diffusion theory. However, the interplay between solute diffusion and grain/phase boundary kinetics, while well understood at an atomic level, is difficult to model at the meso-scale. It is models at this length scale, though, that are

of central importance in making quantitative predictions of morphological evolution. This is certainly the case in engineering applications of solidification, precipitation, allotropic transformation, heat treatment of metals, and recrystallization of amorphous structures.

Analytical models have been developed that make some union between the short-scale interactions and long-scale interactions realized in the formation of polycrystalline grain structure. As is the failing of theoretical constructs, only the most idealized systems are approachable by these models. Often precise experimentation on polycrystalline systems of sufficient simplicity and similarity to analytical models is unrealizable. Furthermore, experimentation without the guidance of predictive tools is costly and unproductive. With the recent revolution in the power of computers, numerical methods of study are being developed to overcome the deficiencies of both theoretical analysis and experimental exploration of microstructural evolution.

A number of simulation techniques have been developed for the simulation of anisotropic grain growth [36], diffusion-driven grain transformations [20], and solute drag phenomena [25]. These can be generally categorized into either deterministic/continuous methods, or probabilistic/discrete methods. Deterministic methods involve solving systems of differential equations, such as the diffusion equation. Prob-

abilistic methods typically use Monte Carlo simulation to model events in a manner consistent with statistical mechanics. A major handicap to these efforts is the absence of experimental data on the scale appropriate to the interactions studied. Parameters used in these models such as free energy, diffusivity and interfacial energy can only be gleaned arbitrarily from measurements such as calorimetry and cross sectional energy dispersive spectroscopy (EDS). By combining the theories of analytical models with results from independent numerical models, the concerted goal is to predict whatever indirect measurements are possible and thereby validate our understanding of practical materials science.

Thin film photovoltaics is one industrial application that would benefit from a predictive grain evolution tool. It is not well understood why the desired electrical properties of polycrystalline photovoltaics are achieved only within a narrow range of process conditions. It is conjectured that grain size, grain boundary diffusion and bulk grain diffusion of dopants each play a role. The anneal process for reaching the optimal microstructure is arrived at by painstaking experimental development. Having a simulation test platform for different anneal conditions would eliminate taxing film growth and measurement.

Motivated by the issues discussed above, this thesis poses and answers the fol-

lowing question:

Thesis Question: Is it possible to construct a discrete, probabilistic simulation of grain and precipitate boundary evolution in the presence of a diffusing solute?

This thesis research develops the digital kinetics model as a valid numerical approach for the simulation of grain growth and precipitation on a level comparable to models adapted from the deterministic sharp-interface and phase-field theories. A similar discrete, probabilistic paradigm was created by P. Liu[2],[3] for simulating the influence of stress on an evolving microstructure. In the present research, driving forces from the reduction of the system free energy and grain boundary energy are considered. The digital kinetics model employs Monte Carlo sampling to handle both solute diffusion and phase evolution. The emphasis of the discrete approach is to accurately numerically simulate the motion of grain boundaries with a realistic description of the sharp boundary profile on the meso-scale. The digital kinetics model is intended to accurately and efficiently handle highly localized phenomena such as solute drag effects as well as long range effects of bulk and grain boundary diffusion. The motivation behind developing the digital kinetics model is to simulate more complex system configurations than is possible with sharp-interface theory while

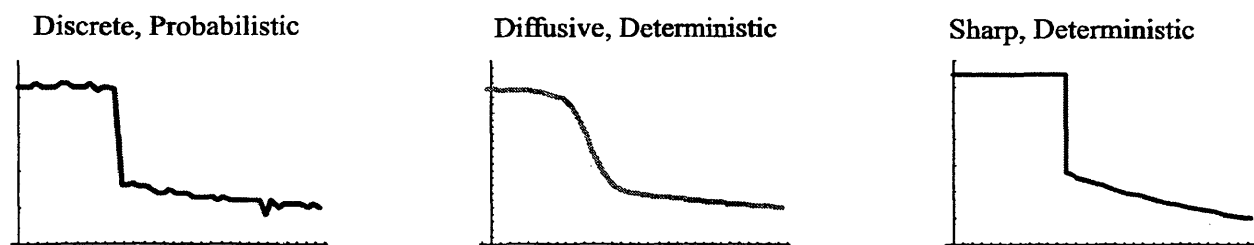


Figure 1.1: Examples of cross-sectional solute concentration profiles resulting from simulations based on the digital kinetics, phase-field and sharp-interface models, respectively.

retaining the sharp-interface description of boundaries in contrast to the phase-field model. Figure 1.1 demonstrates examples of concentration profiles produced by the three models.

The physics behind diffusion and phase evolution as well as a literature review are presented in Chapter Two. In Chapter Three the sharp-interface theory is presented and adapted for grain coarsening and precipitation. Chapter Four introduces the phase-field model in a non-standard way and presents models adapted for precipitation and grain growth. The digital kinetics theory and numerical routine is presented in Chapter Five. The results from the three approaches are compared in Chapter Six. Chapter Seven discusses the successes of the digital kinetics model as well as

the limitations.

CHAPTER 2

BACKGROUND

A review of the basic laws governing diffusion and microstructural properties not only serves as a foundation for the modeling methods developed in further chapters; it also demonstrates the dichotomy between discrete-event mechanisms and deterministic phenomena inherent to the problems of grain growth and precipitation. First the fundamentals of diffusion are introduced and then the more intricate physics behind grain boundary migration is explored.

2.1 Diffusion

The mechanics of solute diffusion through a bulk grain is governed by Fick's second law:

$$\frac{\partial C}{\partial t} = D \frac{\partial^2 C}{\partial z^2} \quad (2.1)$$

The diffusion constant D is a measure of solute flux, as defined in Fick's first law ($J = -D \partial C / \partial z$), and has units of $[m^2 s^{-1}]$. This deterministic relationship can be viewed on the atomic scale by observing solute atoms jumping through interstitial sites (interstitial diffusion) or vacant lattice sites (substitutional diffusion). In a simple model for diffusion through a cubic lattice, in which each site has six nearest neighbor sites, with lattice spacing a , the diffusion constant is given by

$$D = \frac{1}{6} \Gamma a^2. \quad (2.2)$$

According to this model the diffusional jumps occur at a rate $\Gamma[1]$:

$$\Gamma = zv \exp \frac{-\Delta G_m}{RT}. \quad (2.3)$$

The vibration frequency of the lattice is given by v , the number of vacant sites (interstitial or lattice) surrounding any given solute atom is z , while the $\exp(-\Delta G_m / RT)$ term is a measure of jump probability based on the free energy of the solute atom. A successful jump occurs if the solute atom has sufficient thermal energy RT relative to the energy ΔG_m . This energy is the summed work required to move between sites, referred to as the activation energy Q_{act} , and the change in the energy state from one position to another ΔG :

$$\Delta G_m = Q_{act} + dG. \quad (2.4)$$

The first term in equation (2.4) is the enthalpy change ΔH caused by the jump process. For substitutional diffusion, the activation energy is roughly constant for lattices of a given crystal structure and bond type. For interstitial diffusion only, the activation energy is proportional to the diffusion constant according to

$$D \propto \exp \frac{-Q}{2.3RT} \quad (2.5)$$

where the factor 2.3 is found by fitting experimental diffusion data for various interstitial solutes [1]

The second term in equation (2.4) is the work required for change of state as given by the Gibbs free energy of the system ($G = H - TS$). The enthalpy term H can be decomposed into internal energy and mechanical energy terms as $H = E + PV$. Additional contributions to the Gibbs free energy come from the atomic components of the system A, B, \dots . The change in free energy per unit volume for a given diffusional change is then:

$$dG = dE - SdT + VdP + \mu_A d\rho_A + \mu_B d\rho_B + \dots \quad (2.6)$$

where μ_A is the molar chemical potential of solute A with concentration ρ_A . Equation (2.6) is written assuming constant volume, valid for condensed phases, in which no chemical reactions occur. The systems that are of interest in this research assume

isothermal conditions—i.e. $dT = 0$ and no mechanical work beyond that which is included in the boundary energy [1]. It should be noted that for these conditions the Gibbs free energy, Helmholtz free energy and internal energy are identical, though the symbol G will continue to be used.

The chemical potential is defined as the proportionality constant relating the contribution of the molar quantity of one solute species to the total Gibbs free energy (Eqn. (2.7)). Figure 2.1 shows typical free energy curves for two stable or metastable phases with increasing mole fraction X_B of solute element B . If the free energy for a particular phase is approximated by a parabolic function as in equation (2.8), then the chemical potential is simply proportional to the concentration (Eqn. (2.9)). Diffusion is a mechanism to drive the free energy to a minimum under constant temperature, pressure and total solute mass.

$$\mu_A = \left(\frac{\partial G}{\partial \rho_A} \right)_{T,P,\rho_B} \quad (2.7)$$

$$G^\alpha \approx \frac{k^\alpha}{2} (X_B - X_0^\alpha)^2 - G_0^\alpha \quad (2.8)$$

$$\mu_A^\alpha = k^\alpha (X_B - X_0^\alpha) \quad (2.9)$$

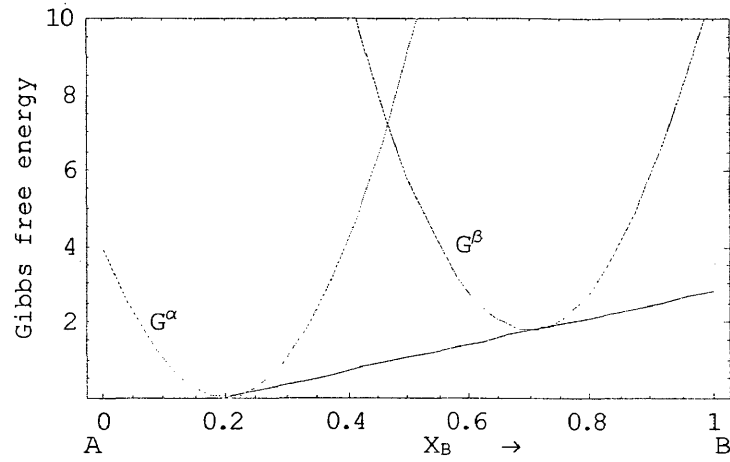


Figure 2.1: Free energy curves for phases α and β in a binary solution of components A and B.

Since solute atoms will diffuse away from regions of higher chemical potential, the driving force for diffusion will be proportional to the gradient of μ_A :

$$f_A \propto \frac{\partial \mu_A}{\partial z} \quad (2.10)$$

2.2 Microstructural Evolution

The mechanisms of solute diffusion are well understood and are in agreement with experimental observations. In contrast, the kinetics of microstructural change, though related to the processes of diffusion, are far less understood due to the com-

plexity of interactions. Two basic mechanisms of microstructural evolution are treated in the present research. Precipitation and grain coarsening are treated as separate phenomena, though much of the developed theory applies generally to both.

2.2.1 Precipitation and Coarsening

Since the present interest is in exploring the common reactions witnessed in annealing solid metal alloys, the phenomena of grain coarsening and precipitation are treated. In a multi-grain system both coarsening and precipitation kinetics would be involved simultaneously, but treating these as separate cases is useful.

Precipitation reactions are defined as interactions between two grains of different composition and chemical phase. In a precipitation transformation, a "grain" with a supersaturated concentration decomposes into a stable configuration of the original phase as well as another phase of different composition. Precipitation can be caused by a change in temperature, allowing a previously stable phase to become supersaturated and metastable, or if a metastable grain has been locked in the matrix, a change in the stress state can trigger the transformation. Two different grains in a precipitation reaction (say of phase α and β) are distinguished by different equilibrium

concentrations ($\rho_{0\alpha}$ and $\rho_{0\beta}$) that show up in equation (2.9) as:

$$\mu_{\alpha} = k(\rho - \rho_{0\alpha})$$

$$\mu_{\beta} = k(\rho - \rho_{0\beta})$$

Grain coarsening is characterized as interactions between two regions of the same composition but different orientation. The diffusivity in one direction through the lattice will vary with different lattice orientation. In terms of the chemical potential, this is realized with different energy gradient constants:

$$\mu_{\theta_1} = k_{\theta_1}(\rho - \rho_0)$$

$$\mu_{\theta_2} = k_{\theta_2}(\rho - \rho_0)$$

where the energy gradient constant varies (k_{θ_1} and k_{θ_2}) between two grains of orientations θ_1 and θ_2 . While both orientations could be equally stable, due to mismatched diffusivities concentration gradients can build up at grain boundaries. Boundary migration can be driven by both the curvature of the grain boundary and by a minimization of the bulk energy.

Boundary migration driving forces from the chemical energy, grain boundary energy, misfit strain energy and temperature gradients can contribute to the precipitation and coarsening kinetics. Temperature gradients can be negligible or significant

depending on the process or controls of the particular system. The effects of temperature gradients will be ignored here. The system is also assumed to be isostatic ($\Delta P = 0$) and in a compressed state ($\Delta V = 0$). As mentioned for diffusion, this set of assumptions means that the Gibbs free energy, the Helmholtz free energy and the internal energy all take the same form. The driving force [1] of boundary migration can be expressed as:

$$\Gamma = -V \Delta G_V + A \gamma + V \Delta G_S. \quad (2.11)$$

Included in equation (2.11) is the bulk free energy density ΔG_V , scaled by the grain volume V , the surface tension of a grain boundary γdA , where γ is the surface free energy along a length of boundary area dA , and strain energy ΔG_S . Strain energy generally cannot be neglected. Modeling strain energy can be quite complex and is the topic of many studies, some of which are summarized below in the literature review. Research performed by P. Liu [2], [3] is the most significant of these since it uses a similar methodology to model strain energy-driven transformations. It is the eventual goal that the present model and the model developed by Liu be combined. With this in mind, the current effort ignores strain energy effects. The remaining factors of bulk energy and boundary energy are treated in the computer models. The details of the model kinetics will be discussed in detail in the following chapters.

The next section lists various driving forces of boundary migration and their relative contribution in typical systems.

2.2.2 Driving Forces of Boundary Migration

The driving forces affecting precipitation and grain boundary migration depend on the fabrication techniques, anneal conditions, compositions and material properties [4]. The driving forces from some sources can be found experimentally, though oftentimes analytical approximations or numerical modeling are needed to explore a particular mechanism. The following list from *Grain Boundary Migration in Metals* [Gottstein, G., page 130] [4] enumerates the various driving forces that have been observed in systems with interface migration.

Chemical driving force One of the most significant and most commonly encountered driving force is due to compositional gradients. The same driving force that induces bulk diffusion is omnipresent in the in-homogenous regions near grain boundaries. The equation $P = RTc \ln c - RT_0 c_0 \ln c_0$ is used to determine the chemical potential contribution to interface motion. The term $RT_0 c_0 \ln c_0$ represents the energy at the maximum solubility temperature. 5% Ag in Cu at $300^\circ C$ will see chemical driving forces of approximately $500 MPa$.

Interface energy The energy of an approximately spherical grain is taken as equivalent to the surface tension of a bubble. A single grain will have a driving force of $P = 2\sigma_b/R$ where $\sigma_b(\sim 0.5J/m^2)$ is the boundary energy and $R(\sim 10^{-4}m)$ is the radius of curvature. Boundary energy driving forces on the order of $10^{-2}MPa$ strive against each other as some grains shrink and others grow. One consequence of the driving force due to interface curvature is that the boundary junctions for a stable grain in two dimensions forms an angle of 120° . Thus a two dimensional grain with fewer than six boundaries will shrink at the expense of grains with greater than six boundaries [1]. The grain boundary energy effect begins to become significant above temperatures of $0.5T_m$.

Stored deformation energy Differences in the defect and dislocation density between grains can provide a strong driving force for interface migration. The driving force is found from the dislocation density ($\rho \sim 10^{15}m^{-2}$), shear modulus ($\mu \sim 10^{11}J/m^3$), and Burgers vector ($b^2 \sim 10^{-19}m$) by $P = \rho\mu b^2/2 \cong 10MPa$. Of course dislocations are removed as annealing progresses.

Elastic energy For coherent and semicoherent boundaries, the most significant driving force can be due to elastic stress. $P = \tau^2/2(1/E_1 - 1/E_2)$ represents the

driving force between two regions of elastic moduli E_1 and E_2 ($\sim 10^5 MPa$) experiencing an elastic stress τ ($\sim 10 MPa$). Forces of $10^{-4} MPa$ are typical.

Surface energy For samples of thin sheets in which a single grain constitutes the thickness, the anisotropy of surface tensions between neighboring grains can contribute $P = 2\Delta\sigma^s/d$ to the driving force. Typical values of surface energy difference $\Delta\sigma^s$ of $0.1 J/m^2$ and crystal thickness d of $10^{-3} m$ can produce a driving force of $10^{-4} MPa$.

Magnetic field Ferromagnetic materials experience interface migration due to magnetic forces at sufficient temperatures. Differences in magnetic susceptibilities $\Delta\chi$ ($\sim 10^{-7}$ at $250^\circ C$), alignments ($\cos^2 \Theta_1 - \cos^2 \Theta_2$ for $0^\circ \leq \Theta \leq 90^\circ$) and the magnetic field strength H ($\sim 10^7 A/m$) combine for $P = \mu_0 H^2 \Delta\chi (\cos^2 \Theta_1 - \cos^2 \Theta_2)/2 \cong 10^{-4} MPa$.

Temperature gradient Typically, thermal energy is dissipated through the lattice at a much higher rate than the time scale of boundary motion. However, thermal sinks and sources as well as significant resistivity differences through grain boundaries can contribute a $T\Delta S$ term to the Gibbs free energy. The driving force can be calculated as $P = \Delta S \cdot 2\lambda\nabla T/\Omega_a$ from the terms of entropy

difference ($\Delta S \cong 8kJ/K \cdot mol$), grain boundary thickness ($2\lambda \cong 5\text{\AA}$), and molar volume ($\Omega_a \cong 10cm^3/mol$). A temperature gradient of $10^4K/m$ will produce a driving force of $10^{-5}MPa$.

Though most of the driving forces listed above can contribute to microstructural evolution in any given system, some can be neglected as miniscule contributions while others, such as magnetic fields, can be ignored as specific to a narrow range of systems. The simulations of precipitation and grain coarsening consider chemical energy and interface energy contributions to the driving forces for boundary migration.

2.2.3 Einstein Relation for Migration

As shown in equation (2.11), the driving forces for grain boundary migration can be expressed as a minimization of free energy. If strain energy effects are ignored, then the motion of grain boundaries is due to the interplay between the mechanical driving force of the surface free energy and the bulk free energy.

Developing the interface migration kinetics for a real system begins with the consideration of a single flat interface between two grains. The grain boundary is the demarcation line between two crystallized regions that differ in phase, orientation, or both. The simplest case to examine is a boundary between identical phases that have

rotated lattice vectors with respect to each other. Small angles of rotation ($< 15^\circ$) produce semi-coherent grain boundaries, for which the developed grain boundary kinetics will not apply [1]. The strain energy produced in angles of rotation greater than 15° can not be accommodated by lattice strain and instead the free energy is minimized by introducing a layer of vacancies to separate the grains. These vacancies offer natural sites for atom migration all along the boundary. The flux of atoms from one grain to another, say grain 1 to grain 2, can be described by

$$J_{1 \rightarrow 2} = A_2 n_1 v_1 \exp(-\Delta G^a / RT) \quad (2.12)$$

where ΔG^a is the activation energy needed for an atom to break away, v_1 is a characteristic vibration frequency of an atom in grain 1, n_1 is the areal concentration of atoms on the edge of grain 1, and A_2 is the 'sticking' coefficient for grain 2 (probability that an atom will not transfer back to grain 1) [1]. A similar flux is found for atoms transferring from grain 2 to grain 1. Converting the net flux to a boundary velocity, a high-angle boundary with a small driving force of ΔG and volume density V_m will travel at a rate V according to:

$$V = \frac{A_2 n_1 v_1 V_m^2}{N_a RT} \exp\left(-\frac{\Delta G^a}{RT}\right) \frac{\Delta G}{V_m} \quad (2.13a)$$

$$V = M \cdot \frac{\Delta G}{V_m} \quad (2.13b)$$

The equivalent relationships of (2.13) demonstrate the duality of probabilistic and deterministic approaches in the boundary migration problem. While equation (2.13a) describes the velocity on the basis of the probability $\exp(-\Delta G^a/RT)$, equation (2.13b) includes the time average of this term in the mobility M . The Nernst-Einstein relation defines: $D = MRT$. Equation (2.13b) implies a linear relation between interface velocity and driving force. The phenomenon of solute drag is seen when, at low impurity concentration, the linearity between velocity and driving force is discontinuous (Figure 2.2). Capturing the effects of solute drag in a theoretical or numerical construct is a major challenge to producing predictive tools that can deal with non-ideality. Next, past efforts to characterize microstructural transformations both experimentally and through theoretical and numerical models are explored.

2.3 Experimental and Theoretical Studies of Grain Boundaries

Surface analysis techniques offer tools for exploring microstructures and experimentally obtaining physical properties of interest. However, as many of the structures of interest are on a micro-scale and are sensitive to destructive measurement techniques, there is a dearth of direct experimental data to verify idealized theories. Most experiments employ high resolution scanning techniques to study structure while the

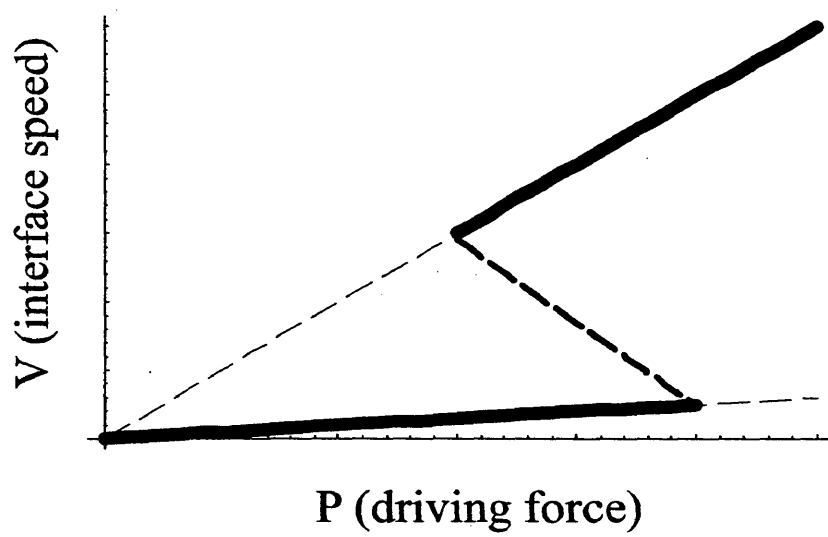


Figure 2.2: Solute drag effect on the relationship between interface velocity and driving force.

experimental study of kinetic processes relies almost entirely on the measurement of indirect and system-averaged parameters. The basic laws of bulk self-diffusion and interdiffusion can be experimentally verified by tracking radioisotopes through thinly-sectioned samples [6], [7], [8].

Experimental investigations on the kinetics in multiphase systems and at grain interfaces are another challenge. Transmission electron microscopy (TEM), scanning electron microscopy (SEM) and energy dispersive X-ray analysis have been used to image microstructures at interfaces [10], [13], [14], [15]. TEM was employed to study age hardening of Al alloys with cyclical loading in [12], and to investigate the structure of semi-coherent interfaces [9]. High temperature TEM studies revealed that three different reactions occur in the formation of θ -phase crystals in Al-Cu alloys [11]. Calorimetry can provide a rough measure of interface energies [16]. The most intensive efforts of studying the rates of grain boundary migration portend to the phenomena of diffusion induced grain boundary migration (DIGM) and diffusion-induced recrystallization (DIR). The boundary between a large grain and a region of recrystallized alloy in diffusion couples has been studied using optical microscopy, TEM, SEM and electron probe micro-analysis (EPMA) [17], [18], [19], [20]. The different researchers found disparate activation energies which has led to a conclusion

that there are different stages of grain boundary migration involved, though there is still disagreement about the mechanisms and driving forces. By studying the growth of Al-Cu allotriomorphs (precipitates that grow out of a grain boundary) under an electron microscope Aaron and Aaronson determined that the growth rates were too fast to be accounted for by bulk diffusion and derived the interphase boundary diffusion coefficient to be $0.23 \exp(-12,800/RT)$ [21]. An impressive experiment using a scanning x-ray to track the migration of a tilt boundary produced some of the most direct measures of activation enthalpies [22]. The underlying weakness of these experimental studies is their inability to capture the effects of one driving mechanism at a time.

Theory-based models restricted by conditions such as the conservation of mass, momentum or energy have been developed that describe various observed phenomena. In Gibb's Gedanken experiment, a system of two abutted grains was treated as three separate phase regions and the Gibbs free energy is evaluated in each region. The boundary is treated as a third 'phase' region which has an additional grain boundary energy term. A supersaturation term for solute in the boundary region is found which is inhibitive to the driving force. This method is effective for explaining solute drag phenomena though it does not accurately predict the severe behavior seen in

Figure 2.2.

A model of drag behavior using a very localized boundary-impurity interaction was developed by Cahn and independently by Lücke and Stüwe [25]. The impurity concentration at the boundary is described by $C_0 = C_\infty e^{-E_0/kT}$. The heat of segregation (the energy derived from transferring impurities from the lattice to the boundaries) E_0 can be positive or negative depending on whether impurities are repulsed or attracted to the grain boundary. Short of phase separation, most systems lower their free energy by concentrating impurities at the boundaries ($E_0 < 0$). Therefore, though the overall concentration of impurities in bulk systems may be negligible, the local concentration at the boundaries is often significant. It is this locally high concentration of impurities that slows down the boundary. As the boundary migrates, the boundary impurities must either diffuse along with the boundary or be re-incorporated into the bulk lattice. If the impurities migrate along with the boundary, then a portion of the boundary driving force must be devoted to ‘dragging’ the impurities along, thus slowing boundary migration rate. At a sufficiently high driving force, the boundary is able to break away from the impurities and travel at the rate predicted for a pure material. Indeed, since pure enough materials are seldom attainable, ‘pure’ grain boundary migration rates are experimentally found by

extrapolating from fast-moving boundaries [4]. The predictions of the Cahn, Lücke and Stüwe model are included in Figure 2.4. The development of the fully discretized digital kinetics model is motivated by the desire to have a numerical approach that can accommodate the localized forces contributing to solute drag.

Additional theoretical developments address predictions of boundary rates in a variety of systems. The effective diffusivity of combined bulk diffusion and grain boundary diffusion is discussed in [23]. Parabolic rate constants have been used to predict layer growth in diffusion couples [24]. Continuum models have been developed that tackle solute drag phenomena by incorporating the segregation of solute and vacancies at grain boundaries [26], as well as thermodynamic considerations [27]. An alternative explanation of the solute drag effect as a metastable state of thermodynamic equilibrium was presented in [28] and the effect of drag on grain structure is examined in [29]. Models incorporating coherency strain and chemical driving forces models have been developed to describe the phenomenon of diffusion-induced grain boundary motion (DIGM) motion in which boundary migration is driven by a chemical potential gradient near the boundary [30]. Improvements were later made to this model including supersaturated mass transport in boundaries and at free surfaces [31].

The sharp-interface theory gives an analytical solution for the kinetics of a moving grain boundary. This is accomplished by balancing the configurational forces on either side of an infinitely sharp interface [5]. The sharp-interface solution is treated as the true solution for the idealized system. Beyond ideality, the sharp-interface model is difficult to implement numerically due to the singularity at the boundary. The use of the sharp interface theory is usually reserved for simple geometries. The theory behind the sharp interface model will be developed in detail in the Chapter Three.

2.4 Numerical Modeling of Grain Boundary Motion

The analytical models of grain boundary migration behavior are developed for simple grain interface geometries based on continuum theory after several simplifications and limitations are imposed. Numerical models are needed to handle complex systems and processes governed by localized potentials such as solute drag. A numerical model can be developed from deterministic equations or from discrete event kinetics employing Monte Carlo sampling. The phase-field model and the Ising/Potts models are chosen examples of these two approaches that are both currently being developed by the solid state simulation community. The Ising/Potts model was

adapted for the digital kinetics model. Literature examples of each are presented here.

2.4.1 Phase-field: Continuum-theory approach

Continuum based numerical models such as the phase-field model attempt to describe grain boundaries as diffuse changes of state over a finite width. As a tool for investigating microstructure, the phase-field is built on the meso-scale. As such, individual atoms are grouped together and considered in terms of atomic densities. The distinguishing feature of the phase-field approach is the continuity of properties throughout the system. Behavior at the boundaries is governed by partial differential equations that are discretized into small enough finite elements to satisfy the stability of continuity assumptions.

In the phase-field model, the variation in lattice properties such as equilibrium concentration and diffusivity are linked to an order parameter - the phase. The phase ($\varphi_n(x, y, z)$) is viewed as a field describing the degree of membership of each point in the lattice to a given lattice structure or orientation as denoted by the subscript n . A separate phase-field plane is needed for each possible lattice structure or orientation. At each point in the lattice, the phase parameters from all planes sum

to unity ($\sum_n \varphi_n(x, y, z) = 1$). Thus a point that is far from any grain boundaries or dislocations will have full membership in one phase-plane only and zero membership in all other planes. However a point near a boundary that is affected by more than one lattice orientation has significant membership in two or more phase-planes. In this manner, the properties at a point are not relegated to either the bulk or the boundary properties. A continuum of physical properties is realized. The phase-field equations can be found directly from the thermodynamics and mass balance equations of diffusion and grain motion as will be seen in Chapter Four. Thus, physical values can be applied to the model and no calibration of time scale or length scale should be necessary.

The major shortfall of the phase-field model is the additional computation required compared to the Potts model. While only one array is needed to represent the order parameter at each point in a Potts model, $n_{total} = p \times Q$ arrays are required for phase-field systems with p possible lattice structures and Q possible lattice orientations. A binary system with two phases needs around 30 planes to sufficiently represent the infinite number of possible phase-orientation combinations [32]. Moreover, to accurately model a grain boundary in the phase-field model without losing phase-field continuity, roughly twice the resolution is required compared to the Potts

model. Fan et.al. modeled a circular grain with isotropic mobility and demonstrated significant deviation from theory for spatial resolutions that relegate fewer than seven grid points to grain boundary regions [40]. Like the Potts model, the phase-field model mis-predicts diffusivities since effects from bottlenecks and triple junctions are neglected.

Unlike the Potts model, the phase-field model is proven to introduce no anisotropy due to discretization of the lattice. The phase-field model is a favorite tool for investigating diffusion in evolving microstructures. The free energy function becomes a function of position. The chemical potential variations drive diffusion, thus the diffusion is an integral part of the phase-field kinetics. The spatially varying chemical potentials can result in solute segregation at grain boundaries. This makes it a candidate model for studying solute drag, though not ideal due to the diffuse description of interfaces. Figure 2.3 shows an example of phase-field calculations that incorporates solute drag effects [39].

The phase-field model is an exciting and useful tool because the diffusion of solute and the evolution of the microstructure are coupled together in the developed rate equations. The rate of diffusion and the rate of grain boundary migration are both controlled by the intrinsic properties assigned to each phase (equilibrium

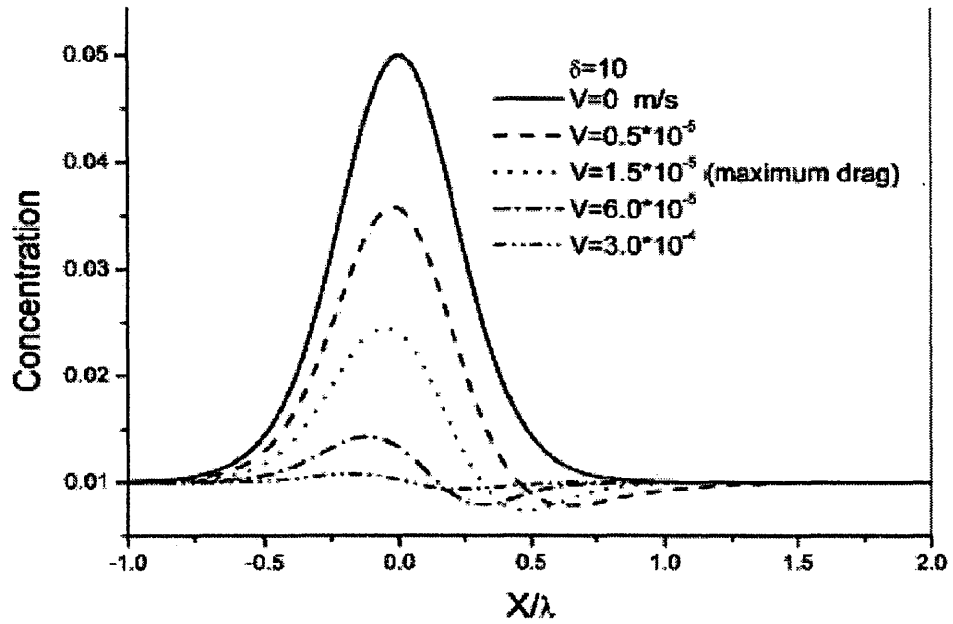


Figure 2.3: The concentration profile across a grain boundary as determined from the phase-field model created by Cha et.al.[39]. The distance is scaled with sample thickness λ .

concentration, energy gradient constant and system-wide solute mobility). For a single grain, the phase-field model reduces to Fick's second law.

Landau developed a model for ferromagnetic transformation using continuous order parameters to describe magnetization. Evolution of this model has brought us to multiphase-field models used for the microstructure studies of today. Swiler, Tikare and Holm found complementary results through use of both a diffusion-coupled phase-field model and a discrete model[32]. Multiple-phase-field models have been developed to simulate anisotropic grain growth [36] and alloy solidification [33], [34], [35]. Atomic mobility was a functional parameter in a phase-field model in [37]. Mecozzi et. al. were able to get satisfactory results in modeling austenite to ferrite transformations in comparison to dilatometry and laser scanning confocal microscopy observations [38]. Attempts have been made to modify the phase-field model with segregation potentials to study solute drag [39].

Due to the immense size scale difference between grain boundaries ($\approx 10nm$) and bulk grains ($\approx \mu m$), a continuum scheme is either inaccurate or unmanageable beyond the nano-scale. Fan et. al. [40] determined that a spacial discretization less than $\lambda/5$ (boundary width $\lambda \cong 10nm$) is needed at the boundaries otherwise the continuous equations become unstable and produce meaningless solutions. This requirement for

a greater number of lattice points becomes a liability in terms of CPU time. Aside from the computational intensity, the drawbacks of the phase-field model are the same as the Gibbs treatment above; supersaturated boundary concentrations and local interaction potentials cannot be accommodated by the continuity requirement. Aaron and Aaronson showed that boundary diffusion must be incorporated in models as bulk diffusion assumptions mis-predicted the growth rate of grain boundary precipitate by several orders of magnitude[21]. A second problem that limits the usefulness of the phase-field model is that the parameters used to set up the model have no direct relationship to properties that can be measured. Hoyt et. al. resorted to using an atomistic model of solid-liquid interfaces to find phase-field mobility terms for solid Cu-Ni alloys[41].

For the purposes of the present research the phase-field model was used to simulate precipitation and grain coarsening in a two grain system incorporating diffusion of a single solute species. Results from the phase-field models are compared to the predictions of the sharp-interface theory and the digital kinetics results.

2.4.2 Discrete Models

Models based on sets of continuous equations are imperfect and unstable predictors of the dynamics at grain boundaries since boundary interfaces are essentially singularities. If the discretized continuous field description is abandoned in favor of individual lattice sites, the system is nothing more than interactions between singularities. The infinitely sharp grain boundaries used in the discrete models are a more accurate description of boundaries captured by scanning electron microscopy than the phase-field treatment [19], [20].

Monte Carlo sampling is used to drive discrete models. If the sampling scheme is set up correctly then a collection of discrete trials will reproduce the same results as continuous models over large enough time domains. Monte Carlo sampling might be used in a modeling routine that involves:

1. Choosing a site at random from $N \times N$ sites in a lattice.
2. Calculating the probability of a transformation at the site based on the driving force: $\gamma = \gamma_0 \exp(-F_{total}/kt)$.
3. Comparing this probability to a randomly generated number.

This probabilistic scheme can produce different results for a given set of system

parameters in contrast to the deterministic sharp-interface and phase-field models which always produce the same result for one set of parameters. This random nature can be both a virtue and a liability. Results from a probabilistic model must be time-averaged in order to accurately compare them with results from a deterministic model. However, the probabilistic scheme can be a more accurate description of experimentally observed phenomena, such as diffusion and interface migration.

Discrete, Monte Carlo-based schemes are used for both the diffusional and microstructural transformations in the digital kinetics model. The diffusion scheme in the digital kinetics model is borrowed and modified from the atomistic model of diffusion while the phase evolution scheme comes from Ising/Potts models. Both of these modeling techniques are introduced below and are expanded in detail in the subsequent chapters.

2.4.2.1 Molecular Dynamics Diffusion

The atomistic or cellular automaton model that tracks the motion and state of individual atoms through a lattice falls under the category of molecular dynamics. Molecular dynamics methods operate on the atomic length scale and are based on inter-atomic potentials such as the Lennard-Jones potential. The embedded atom

method (EAM) extends the description of atomic interaction beyond the bonded pair formulation of quantum mechanics [41]. The atomistic model of Hoyt mentioned above was used to investigate the solidification of an alloy system from which the boundary mobility rate was determined and accurate diffusivities were calculated. In [43], the grain boundary energy was calculated from the misorientation of the abutted grains and in this way highlighted the premise that different misorientations have different mobilities. This work also indicated that more than 64 discrete lattice orientations are needed to find boundary migration rates that are not dependant of the degree of discretization. Efficient three dimensional cellular automaton models have been created [44] and improved by only applying transfer algorithms at boundary interfaces [45]. Discrete atomic diffusion across a curvature-driven boundary was investigated in [46].

The key constraint of the atomistic model is the size constraints of atomic scaling and the time scale of interactions. Typically only a single boundary interface is considered. Massive computing power is needed to handle the evolution of a system with more than a single real-size grain. In the digital kinetics model, this constraint will be circumvented by using the same mechanisms while considering discrete amounts of concentration in place of individual atoms. This approach was validated based on

comparisons with predictions of the diffusion equation as is seen in Chapter 6.

2.4.2.2 Ising/Potts Approach to Phase Evolution

Discrete approaches such as the Ising model or the Potts model describe a grain boundary as a discontinuous interface with step changes in properties. These approaches preclude the use of continuum theory-based dynamics and must rely on probability sampling to predict dynamic behavior. Discrete events such as described by equation 2.3 proceed after running the gauntlet of a Monte Carlo algorithm. The Potts model is a general description of a multiphase system while the Ising model is a specialized description of a two phase system. The Ising model will be adopted in the digital kinetics model.

In the Ising/Potts model, each lattice site belongs to only one phase (representing structural phases and orientations). The advantage of this approach over the phase-field approach is the reduction of the complexity and hence computation time of the algorithms. The complete discretization of the phase allows for infinitely sharp interfaces and hence more localized interactions, making the Ising/Potts models more promising approaches for accurately predicting solute drag behavior.

Mendelev and Srolovitz investigated solute drag with an Ising model in which

interstitial solute atoms diffuse via an atomistic algorithm while lattice sites switch phase according to Monte Carlo sampling [48] (Figure 2.5). They were able to produce a closer reproduction of observed solute drag (Figure 2.2) than the analytical descriptions as seen in Figure 2.4. This approach is highlighted as it most closely resembles the digital kinetics diffusion scheme developed in this thesis. The contrast is in the size and time scale, the diffusion algorithm, and the complexity of systems which can be accommodated.

In the simulation by Mendeleev and Srolovitz, the diffusion and boundary migration rates were coupled by a non-dimensionalized relative migration term $\nu = fD\tau/a^2$ where f is a geometric factor which depend on the lattice type, D is the impurity diffusivity, τ is the time step and a is the lattice spacing. The parameter ν is chosen less than unity such that for every time step that the diffusion algorithm is run, the phase-evolution algorithm is run for $1/\nu$ steps. A drawback of the Potts model is that in order to assign special properties to a grain boundary, such as increased diffusivity and equilibrium solute levels, at least one lattice site must be used to define the location of the boundary. This fixes the boundary width to $1/L$ in a lattice of L sites. For typical simulations the ratio of boundary width to grain size (2.5×10^{-3}) is still too high compared to real materials (10^{-4}) [32]. This limitation is still an improve-

ment over the boundary width ratio of a much larger typical phase-field simulation (5×10^{-3}).

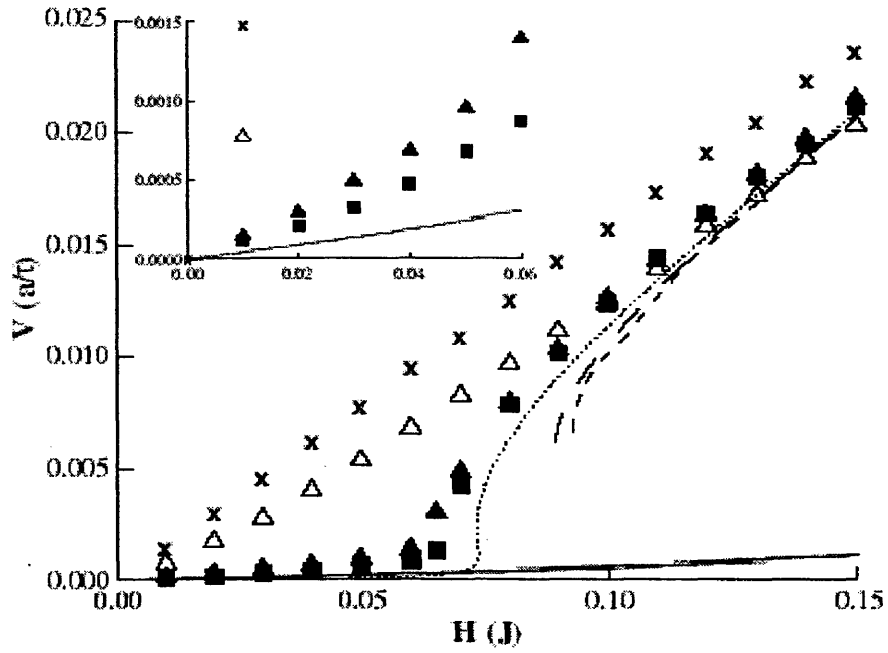


Figure 2.4: Results of Ising-model phase evolution/atomistic diffusion showing solute drag effects of impurities from Mendeleev and Srolovitz[48]. Symbols are model results, x's are results for no impurities, other symbols for increasing impurity concentration. Dashed lines are predictions from Cahn-Lücke-Stüwe analytical model.

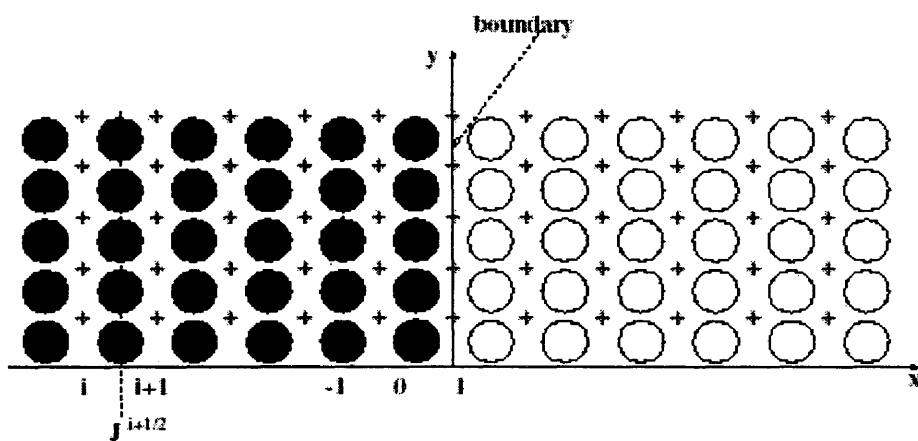


Figure 2.5: The system of interstitial solute atoms (circles) and lattice sites (crosses) used by Mendeleev and Srolovitz for Potts model simulations.

CHAPTER 3

SHARP-INTERFACE MODEL

The sharp-interface theory gives us the most accurate solution to the kinetic relationship of interface motion. It is derived from a set of equations that balance the configurational forces[5]. While the sharp-interface theory is treated as the true solution to interface kinetics, several assumptions must be made that require a simplified system and it is therefore not a good candidate for development into a numerical model. The sharp-interface theory was adapted to create a set of predictions that are used to validate the phase-field and digital kinetics models for specific systems. Since the phase-field and digital kinetics models were developed for a two-dimensional lattice with boundary surface curvature effects, the sharp-interface theory is implemented in an axisymmetric system. In this way, the sharp-interface can be derived for only one dimension yet related to the results of two-dimensional circular grains from the numerical models. The sharp-interface theory does not couple solute diffusion and interface kinetics as the phase-field model does, so steady state conditions

are assumed for the solute profile at all times. This condition can be mimicked in the phase-field and digital-kinetics models by adjusting the mobility of solute diffusion to be much greater than the rate of motion of the interface.

All governing equations will be non-dimensionalized to allow a one-to-one comparison with the non-dimensionalized phase-field model. Appendix A shows that the sharp-interface theory is indeed recovered by the phase-field model in the limit as the interface thickness goes to zero. The configurational force balance equations for the sharp-interface theory are derived using the terms below. The $\tilde{}$ symbol above a term means that it has not been non-dimensionalized.

$\tilde{\rho}$ = solute mass density

$\tilde{\mu}$ = chemical potential of solute

$\tilde{\varepsilon}$ = internal energy density

$\tilde{\sigma}$ = interfacial energy, assumed to be constant

$\tilde{\mathbf{j}}$ = mass flux density of the solute

$\tilde{\Gamma}$ = normal component of an effective configurational force

\tilde{V} = interface speed normal to the interface

\tilde{V}_m = interface speed tangent S and normal to ∂S

The system postulates of mass balance, configurational force balance, dissipation

imbalance, and continuity of the chemical potential are then:

$$\begin{aligned}
\left\{ \int_P \tilde{\rho} dv \right\}^\bullet &= - \int_{\partial P} \tilde{\mathbf{j}} \cdot \boldsymbol{\nu} da & (3.1) \\
\int_{\partial S} \tilde{\sigma} \mathbf{m} dl + \int_S \tilde{\Gamma} \mathbf{n} da &= \mathbf{0} \\
\left\{ \int_P \tilde{\varepsilon} dv + \int_S \tilde{\sigma} da \right\}^\bullet &\leq - \int_{\partial P} \tilde{\mu} \tilde{\mathbf{j}} \cdot \boldsymbol{\nu} da + \int_S \tilde{\Gamma} \tilde{V} da + \int_{\partial S} \tilde{\sigma} \tilde{V}_m dl \\
[\tilde{\mu}] &= 0
\end{aligned}$$

Here $[*]$ indicates the jump in a quantity across the interface and a superscript \bullet indicates a time derivative. The vectors \mathbf{m} and \mathbf{n} are bi-normal and normal to the interface, S , and $\boldsymbol{\nu}$ is the outer normal to the boundary, ∂P , of the region P . In the bulk material, the localizations of these equations are standard, but across interfaces one finds that

$$[\tilde{\rho}] \tilde{V} = [\tilde{\mathbf{j}} \cdot \mathbf{n}] \quad (3.2)$$

$$\tilde{\sigma} \tilde{\kappa} + \tilde{\Gamma} = 0 \quad (3.3)$$

$$\left([\tilde{\varepsilon}] - \tilde{\mu} [\tilde{\rho}] - \tilde{\Gamma} \right) \tilde{V} \geq 0 \quad (3.4)$$

where $\tilde{\kappa}$ is the mean curvature of the interface. It is assumed that the bulk fields can depend on both $\tilde{\mu}$ and $\nabla \tilde{\mu}$ while the surface field can depend on $\tilde{\mu}$. Then, using a Coleman-Noll argument[50],

$$\tilde{\Gamma} = [\tilde{\varepsilon}] - \tilde{\mu} [\tilde{\rho}] + \tilde{\beta} \tilde{V} \quad (3.5)$$

where $\tilde{\beta} \geq 0$. In other words, . The form of $\tilde{\varepsilon}$ and $\tilde{\mu}$ cannot be known until a choice is made to either model precipitation or grain coarsening.

The solution to the chemical potential profile can be found by assuming a piecewise solution to the diffusion equation in cylindrical coordinates. Once the chemical potential profile is determined, the concentration profile is found from the specific relationship between the chemical potential and concentration. Fick's law of diffusion in cylindrical coordinates is written:

$$\rho_r^\bullet = M \frac{1}{r} \frac{\partial}{\partial r} \left(r \frac{\partial \mu}{\partial r} \right) \quad (3.6)$$

The general solution to the steady state condition $\rho_r^\bullet = 0$ is $\mu(r) = C_1 \ln r + C_2$ with arbitrary constants C_1 and C_2 . The only profile that can be applied to the interior of the grain without introducing a singularity at $r = 0$ is a constant chemical potential.

The profile expression for the chemical potential of the exterior lattice is solved by assigning Dirichlet boundary conditions $\rho(R) = \rho_R \equiv \text{constant}$:

$$\mu(r) = \begin{cases} C_{in2} & ; \quad \text{for } r \leq s \\ C_{out1} \ln r + C_{out2} & ; \quad \text{for } s < r \leq R \end{cases} \quad (3.7)$$

The form of the internal energy and the remaining constants in (3.7) cannot be found until conditions are assigned at the boundary and interface. Now the sharp interface model will be adapted to simulate precipitation and grain coarsening.

3.0.3 Precipitation

For the phenomena of precipitation the chemical potential and bulk energy are related to the concentration by:

$$\tilde{\mu} = \begin{cases} \tilde{k}(\tilde{\rho} - \rho_m) & ; \text{ matrix} \\ \tilde{k}(\tilde{\rho} - \rho_p) & ; \text{ precipitate} \end{cases} \quad (3.8)$$

$$\tilde{E} = \begin{cases} \frac{\tilde{k}}{2}(\tilde{\rho} - \rho_m)^2 & ; \text{ matrix} \\ \frac{\tilde{k}}{2}(\tilde{\rho} - \rho_p)^2 & ; \text{ precipitate} \end{cases} \quad (3.9)$$

where \tilde{k} is the energy gradient constant and ρ_m and ρ_p are the equilibrium concentrations in the bulk matrix and precipitate grain, respectively. For precipitation, the dissipation inequality of equation (3.4) is satisfied strictly by $\tilde{\beta} = 0$ and the configurational force balance is simply

$$[\tilde{\varepsilon}] - \tilde{\mu}[\tilde{\rho}] = -\tilde{\sigma}\tilde{\kappa} \quad (3.10)$$

which is sometimes referred to as the *interface equilibrium condition*.

3.0.3.1 Non-dimensional Form of Equations

The system is now non-dimensionalized by introducing l and c as the characteristic length and speed, respectively, and by using the following relationships:

$$\begin{aligned}
 \tilde{\rho} &= \rho(\rho_p - \rho_m) + \rho_m & (3.11) \\
 \tilde{\mu} &= \mu \tilde{k}(\rho_p - \rho_m) \\
 \tilde{\Gamma} &= \Gamma \tilde{k}, \quad \tilde{\sigma} = \sigma \tilde{k} l \\
 \tilde{M} &= \frac{M l c}{\tilde{k}}, \quad \tilde{V} = \frac{V}{c}
 \end{aligned}$$

This gives the non-dimensional equations for the sharp-interface kinetics of bulk-controlled precipitation:

$$\begin{aligned}
 \rho^\bullet &= M \Delta \mu & (3.12) \\
 \mu &= \begin{cases} \rho, \text{ matrix} \\ \rho - 1, \text{ precipitate} \end{cases}
 \end{aligned}$$

with interface jump conditions of

$$[\mu] = 0 \quad (3.13a)$$

$$[\rho] V = -M [\nabla \mu \cdot \mathbf{n}] \quad (3.13b)$$

$$[\varepsilon] - \mu [\rho] = -\sigma \kappa \quad (3.13c)$$

For precipitation, the rate of boundary migration is controlled by the rate at which the solute diffuses across the interface. The velocity is therefore found from the diffusion equation in (3.2) and equation (3.4) is balanced to equality as shown in (3.13b) and (3.13c), respectively.

At the interface, the chemical potential is given by

$$\mu_T = \rho^+ = \rho^- - 1 \quad (3.14)$$

so that the jump condition for energy can be explicitly written as

$$[\varepsilon] - \mu[\rho] = \rho^+.$$

These are the equations that will be compared directly with the two phase-field models. By solving the interface conditions and imposing boundary conditions (3.7), the interface solutions are

$$\rho^- = 1 + \sigma\kappa \quad (3.15)$$

$$\rho^+ = \sigma\kappa \quad (3.16)$$

$$V(s) = \frac{M\kappa(\rho_R - \sigma\kappa)}{\ln R\kappa} \quad (3.17)$$

and if the curvature is $\kappa = 1/s$ then the concentration profile is

$$\rho(r) = \begin{cases} \rho^- & ; \text{ for } r \leq s \\ \left[\frac{\sigma}{s} \ln \frac{R}{r} + \rho_R(\ln \frac{r}{s}) \right] / \ln \frac{R}{s} & ; \text{ for } s < r \leq R \end{cases}$$

3.0.3.2 Equilibrium Area

One prediction that falls out from the sharp-interface solution to the precipitate problem is an equilibrium grain size. If the conditions at the boundary are instead zero concentration flux then conservation of mass allows us to calculate from an initial system configuration to the equilibrium configuration that matches the conditions (3.15) and (3.16). Since the sharp-interface results will be compared to numerical models run on a square lattice, the system area will be $2R \times 2R$. The system mass balance at s_{init} and s_{eq} is then

$$\begin{aligned} \text{system mass} &= \rho_{init}^+ \times 4R^2 + (\rho_{init}^- - \rho_{init}^+) \times \pi s_{init}^2 = \frac{\sigma}{s_{eq}} \times 4R^2 + 1.0 \times \pi s_{eq}^2. & (3.18) \\ s_{eq} &= -(24\pi R^2 \rho_{init}^+ + 6\pi^2 (\rho_{init}^- - \rho_{init}^+) s_{init}^2 + \\ & 2^{-\frac{1}{3}} \left(36\pi R^2 \sigma + \sqrt{1296\pi^2 R^4 \sigma^2 - 12\pi (4R^2 \rho_{init}^+ + \pi (\rho_{init}^- - \rho_{init}^+) s_{init}^2)^3} \right)^{\frac{1}{3}} \end{aligned}$$

The equilibrium grain size as a fraction of the total system area is then

$$\text{area fraction} = \frac{\pi s_{eq}^2}{4R^2}. \quad (3.19)$$

3.0.4 Grain Coarsening

Next an expression for the chemical potential is chosen that is specific to the phenomena of grain coarsening. The internal energy and chemical potential take the form:

$$\tilde{\mu} = \begin{cases} \tilde{k}_m \tilde{\rho} & ; \text{ bulk matrix} \\ \tilde{k}_p \tilde{\rho} & ; \text{ interior grain} \end{cases} \quad (3.20)$$

$$\tilde{E} = \begin{cases} \frac{\tilde{k}_m}{2} \rho^2 & ; \text{ bulk matrix} \\ \frac{\tilde{k}_p}{2} \rho^2 & ; \text{ interior grain} \end{cases} \quad (3.21)$$

In the case of coarsening, the process is limited only by the interface motion such that $\tilde{\mathbf{j}} \cong 0$ in equation (3.2) on the time scale of microstructural evolution. The interface velocity is then found from the dissipative inequality where $\tilde{\beta} > 0$.

3.0.4.1 Non-dimensional Form of Equations

The non-dimensionalization of energy and chemical potential is simplified with the ratio of energy gradient concentrations expressed as $\tilde{k}_m/\tilde{k}_p = (1 + K_n)$ for direct comparison to the parameter used in the phase-field model ($K_n = \tilde{k}_m/\tilde{k}_p - 1$). The

non-dimensional relationships equivalent to (3.11) are:

$$\begin{aligned}
\tilde{\rho} &= \rho \tilde{\rho}_0 & (3.22) \\
\tilde{\mu} &= \mu \tilde{k}_m \tilde{\rho}_0 \\
\tilde{\Gamma} &= \Gamma \tilde{k}_m, \quad \tilde{\sigma} = \sigma \tilde{k}_m l \\
\tilde{M} &= \frac{M l c}{\tilde{k}_m}, \quad \tilde{V} = \frac{V}{c}
\end{aligned}$$

The units of concentration in equation (3.22)₁ are carried by the constant $\tilde{\rho}_0$ such that $|\tilde{\rho}_0| \equiv 1$. The non-dimensionalized form of chemical potential is now:

$$\mu = \begin{cases} (1 + K_n)\rho & ; \text{ bulk matrix} \\ \rho & ; \text{ interior grain} \end{cases} \quad (3.23)$$

For grain coarsening, the boundary migration rate is controlled by rate of restructuring and is independent of the diffusion equation. The condition of $\tilde{\mathbf{j}} \cong 0$ implies that the chemical potential profile (3.7) is piece-wise flat ($C_{out1} = 0$). The velocity of the interface is given by the inequality of (3.4).

$$[\mu] = 0 \quad (3.24a)$$

$$[\rho]V = -M(0) \quad (3.24b)$$

$$V = M([\varepsilon] - \mu[\rho] - \sigma\kappa) \quad (3.24c)$$

The interface jump conditions interface of (3.13a) still applies. At the interface, the chemical potential is given by

$$\mu_T = (1 + K_n)\rho^+ = \rho^- \quad (3.25)$$

so that the jump condition for energy can be explicitly written as

$$[\varepsilon] - \mu[\rho] = \rho^+.$$

Solving the interface conditions and along with the chemical potential profile (3.7) results in the interface solutions:

$$\rho^- = \rho_R(1 + Kn) \quad (3.26)$$

$$\rho^+ = \rho_R \quad (3.27)$$

$$V(s) = M \left(\frac{\rho_R^2 Kn(1 + Kn)}{2} - \sigma\kappa \right) \quad (3.28)$$

Replacing $\sigma = 1/s$, the resulting concentration profile is simply

$$\rho(r) = \begin{cases} \rho^- & ; \quad \text{for } r \leq s \\ \rho^+ & ; \quad \text{for } s < r \leq R \end{cases}$$

The velocity found from the sharp-interface theory is used to compare with the results from the phase-field and digital kinetics models.

3.0.4.2 Implementation

The grain coarsening system does not reach an equilibrium grain size when constrained by conservation of mass as in (3.18). The motion of the interface can be solved starting from an initial configuration of $s = s_{init}$ according to the derivative $V(s) = ds/dt$. At each position s the concentration at the interface is known from (3.27) and (3.26).

CHAPTER 4

PHASE-FIELD MODEL

This chapter introduces the phase-field model following upon the derivation of configurational force balance of the sharp-interface theory. The validity of the phase-field results are checked against the predictions of the sharp-interface theory and then compared with the results from the digital kinetics numerical model in Chapter Six. The derived set of equations are non-dimensionalized as was done for the sharp-interface theory.

Of the two widely used approaches applying the phase-field model[49], the Ginzburg-Landau phase-field model is the more versatile. The Cahn-Hilliard phase-field model uses a piece-wise quadratic energy function to track the solute density as it changes rapidly through a phase boundary. However, the Cahn-Hilliard approach assumes a fixed phase boundary; it is of no use to the present study. The Ginzburg-Landau (GL) system tracks both the solute density and a phase order parameter by means of an elliptic equation.

As shown in Gurtin[49], the GL equations can be derived from a single set of balance principles. The derivation for the GL system in a general setting is shown and then separate models are presented for precipitation and grain coarsening. The new fields are:

$\tilde{\pi}$ = an effective micro-force

$\tilde{\xi}$ = an effective micro-stress

The micro-force balance[5], below, represents a phase-field regularization of the balance of configurational forces:

$$\begin{aligned} \left\{ \int_P \tilde{\rho} dv \right\}^\bullet &= - \int_{\partial P} \tilde{\mathbf{j}} \cdot \boldsymbol{\nu} da & (4.1) \\ \int_{\partial P} \tilde{\xi} \cdot \boldsymbol{\nu} da + \int_P \tilde{\pi} dv &= 0 \\ \left\{ \int_P \tilde{\varepsilon} dv \right\}^\bullet &\leq - \int_{\partial P} \tilde{\mu} \tilde{\mathbf{j}} \cdot \boldsymbol{\nu} da + \int_{\partial P} \tilde{\xi} \cdot \boldsymbol{\nu} \varphi^\bullet da \end{aligned}$$

The same terms are used as defined for the sharp-interface theory with the addition of order parameter term, φ . The differential versions of these equations can be written as

$$\tilde{\rho}^\bullet = -\text{div}(\tilde{\mathbf{j}}) \quad (4.2a)$$

$$\text{div}(\tilde{\xi}) + \tilde{\pi} = 0 \quad (4.2b)$$

$$-\tilde{\varepsilon}^\bullet + \tilde{\mu} \tilde{\rho}^\bullet - \tilde{\pi} \varphi^\bullet - \nabla \tilde{\mu} \cdot \tilde{\mathbf{j}} + \tilde{\xi} \cdot \nabla \varphi^\bullet \geq 0 \quad (4.2c)$$

Allowing all fields to be functions of $\tilde{\rho}$, $\nabla\tilde{\rho}$, φ , $\nabla\varphi$, and using a Coleman-Noll argument[50] gives the following constitutive restrictions:

$$\tilde{\mu} = \frac{\partial\tilde{\varepsilon}}{\partial\tilde{\rho}} \quad (4.3)$$

$$\tilde{\pi} = -\frac{\partial\tilde{\varepsilon}}{\partial\varphi}$$

$$\tilde{\xi} = \frac{\partial\tilde{\varepsilon}}{\partial\nabla\varphi} \quad (4.4)$$

$$\frac{\partial\tilde{\varepsilon}}{\partial\nabla\tilde{\rho}} = \mathbf{0}$$

$$\tilde{\mathbf{j}} = -\tilde{M}\nabla\tilde{\mu}$$

Here the same symbol has been used for both field and constitutive function. These results allow the mass and micro-force balances of equation (4.2b) to be written as

$$\begin{aligned} \tilde{\rho}^\bullet &= \tilde{M}\Delta\left(\frac{\partial\tilde{\varepsilon}}{\partial\tilde{\rho}}\right) \\ 0 &= -\frac{\partial\tilde{\varepsilon}}{\partial\varphi} + \operatorname{div}\left(\frac{\partial\tilde{\varepsilon}}{\partial\nabla\varphi}\right) \end{aligned} \quad (4.5)$$

A specific choice of internal energy is then chosen:

$$\tilde{\varepsilon} = f_0f(\varphi) + \frac{\tilde{K}(\varphi)}{2} [\rho_m^2(1-\varphi) + \rho_p^2\varphi + \tilde{\rho}^2 - 2\tilde{\rho}\rho_m(1-\varphi) - 2\tilde{\rho}\rho_p\varphi] + \frac{\tilde{\gamma}}{2} |\nabla\varphi|^2 \quad (4.6)$$

where f_0 and $\tilde{\varepsilon}$ have the same dimensions. The solute flux becomes a function of

just \tilde{M} , φ , and $\tilde{\rho}$ by defining the chemical potential as a combination of the phase dependant gradient energy function $\tilde{K}[\varphi]$ (where $\tilde{k}_m \geq \tilde{k}_p$) and the effective solute concentration:

$$\begin{aligned}\tilde{\mu} &= \tilde{K}(\varphi) [\tilde{\rho} - \rho_m(1 - \varphi) - \rho_p\varphi] \\ \tilde{K}(\varphi) &= \tilde{k}_m(1 - \varphi) + \tilde{k}_p\varphi\end{aligned}\tag{4.7}$$

The governing equations for phase evolution becomes:

$$\begin{aligned}\tilde{\rho}^\bullet &= \tilde{M}\tilde{K}(\varphi)\Delta\tilde{\mu} = \tilde{D}(\varphi)\Delta\tilde{\rho} - \tilde{D}(\varphi)(\rho_p - \rho_m)\Delta\varphi \\ 0 &= -f_0f'(\varphi) + \frac{\tilde{K}(\varphi)}{2}(\rho_p^2 - \rho_m^2) + \tilde{K}(\varphi)\tilde{\rho}(\rho_p - \rho_m) + \tilde{\gamma}\Delta\varphi\end{aligned}\tag{4.8}$$

Figure 4.1 shows a cross section of the axisymmetric system described in the sharp-interface chapter and the configuration of phase dependant fields.

4.0.5 Non-dimensionalization - General System

The non-dimensional relationships used here are familiar from the sharp interface development (3.11). The choice of scaling relationships will depend on which parameters will be phase dependant. First, the general case is developed in which both the

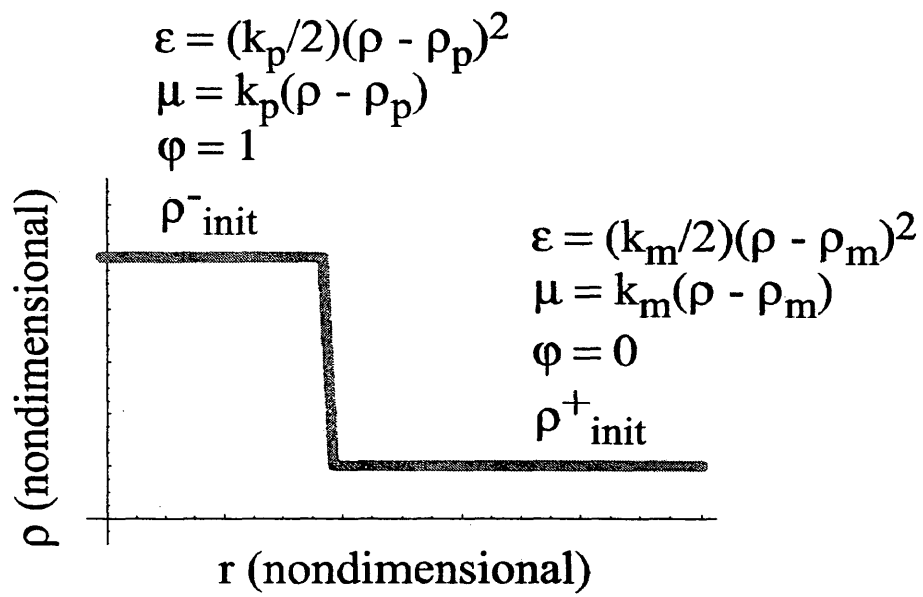


Figure 4.1: Cross sectional view of the axisymmetric system and configuration of phase-field parameters.

gradient energy coefficient and equilibrium solute concentration will change across a grain boundary. For this case, the following relationships will apply:

$$\tilde{\rho} = \rho(\rho_p - \rho_m) + \rho_m \quad (4.9)$$

$$\tilde{\mu} = \mu \tilde{k}_p (\rho_p - \rho_m) \quad (4.10)$$

$$\tilde{M} = Mlc / \tilde{k}_p \quad (4.11)$$

$$\epsilon = \frac{\tilde{k}_p (\rho_p - \rho_m)^2}{f_o} \quad (4.12)$$

$$\tilde{\gamma} = \epsilon^2 f_o l^2 \gamma \quad (4.13)$$

$$K_n = \tilde{k}_m / \tilde{k}_p - 1 \quad (4.14)$$

$$K_f(\varphi) = 1 - 2\varphi K_n \quad (4.15)$$

The non-dimensionalized chemical potential, from (4.7), is now

$$\mu = [1 + (1 - \varphi) K_n] (\rho - \varphi). \quad (4.16)$$

The governing equations for solute and phase evolution get non-dimensionalized and

simplified:

$$\rho^{\bullet} = M\Delta \{[1 + (1 - \varphi) K_n](\rho - \varphi)\} \quad (4.17)$$

$$0 = -f'[\varphi] \epsilon^{-1} + \frac{K_n}{2} \rho^2 + K_f(\varphi)(\rho - 1/2) + \epsilon\gamma\Delta\varphi. \quad (4.18)$$

The exchange energy, $f(\varphi)$, is chosen to be the standard double-well potential,

$$f(\varphi) = \varphi^2(1 - \varphi)^2. \quad (4.19)$$

And the derivative takes the form

$$f'(\varphi) = 2\varphi - 6\varphi^2 + 4\varphi^3. \quad (4.20)$$

>From (4.19) a relationship can be made between the surface free energy term γ and the surface energy from the sharp-interface theory σ :

$$\sigma = \gamma \int_0^1 \sqrt{2f(\varphi)} d\varphi \implies \frac{\gamma}{6} \quad (4.21)$$

4.0.6 Non-dimensionalization - Grain Coarsening

Evaluating the general phase-field model that simulates both grain coarsening and precipitation could be too complex. In order to test the evolution due to a singular phenomena, two specialized phase-field models are developed. For the grain

coarsening system, two neighboring grains with identical phases but different orientations interact ($\rho_p = \rho_m = 0$). If the same scalings of (4.9) were used, then $\epsilon \rightarrow 0$ thus introducing an infinity into the phase governing equation of (4.17). Choosing a new scaling relationship for the solute concentration also requires reforming the term ϵ and the non-dimensionalized chemical potential:

$$\tilde{\rho} = \rho \tilde{\rho}_0 \quad (4.22)$$

$$\tilde{\mu} = \mu \tilde{k}_p \tilde{\rho}_0 \quad (4.23)$$

$$\tilde{M} = M l c / \tilde{k}_p \quad (4.24)$$

$$\epsilon = \frac{\tilde{k}_p}{f_o} \quad (4.25)$$

$$\tilde{\gamma} = \epsilon^2 f_o l^2 \gamma \quad (4.26)$$

$$K_n = \tilde{k}_m / \tilde{k}_p - 1 \quad (4.27)$$

$$\mu = [1 + (1 - \varphi) K_n] \rho. \quad (4.28)$$

The units of concentration in equation (4.22) are carried by the constant $\tilde{\rho}_0$ such that $|\tilde{\rho}_0| \equiv 1$. The governing equations for solute and phase evolution change as well:

$$\rho^\bullet = M \Delta \{ [1 + (1 - \varphi) K_n] \rho \} \quad (4.29a)$$

$$0 = \epsilon^2 \left(-f'(\varphi) \epsilon^{-1} + K_n \frac{\rho^2}{2} + \epsilon \gamma \Delta \varphi \right). \quad (4.29b)$$

In order to accomplish the conditions that match the steady state sharp-interface conditions it is necessary to scale (4.29b) by two orders of ϵ so that on the time scales of interest $\rho^\bullet \implies 0$. The exchange energy (equation (4.19)) remains of the same form.

4.0.7 Non-dimensionalization - Precipitation

For the precipitation version of the phase-field model the orientations are now identical but the equilibrium concentrations differ: $\tilde{k}_m = \tilde{k}_p = \tilde{k}$. The scaling relationships are identical to those of the sharp-interface precipitation (3.11):

$$\tilde{\rho} = \rho(\rho_p - \rho_m) + \rho_m \quad (4.30)$$

$$\tilde{\mu} = \mu \tilde{k}(\rho_p - \rho_m) \quad (4.31)$$

$$\epsilon = \frac{\tilde{k}(\rho_p - \rho_m)^2}{f_o} \quad (4.32)$$

$$\tilde{\gamma} = \epsilon^2 f_o l^2 \gamma \quad (4.33)$$

$$\tilde{M} = Mlc/\tilde{k} \quad (4.34)$$

$$\mu = \rho - \varphi. \quad (4.35)$$

The governing equations for solute and phase evolution for precipitation are:

$$\rho^\bullet = M \Delta (\rho - \varphi) \quad (4.36a)$$

$$0 = -f'(\varphi) \epsilon^{-1} - \frac{1}{2} + \rho + \epsilon \gamma \Delta \varphi. \quad (4.36b)$$

4.1 Numerical Implementation of the Phase-Field Model

4.1.1 Finite Difference Approximation

The phase-field governing equations are solved in a forward-time central-space

finite difference routine within a 2-dimensional lattice of dimensions $i \times j$. The gradients of the chemical potential and the phase are approximated by the expression:

$$\Delta\eta_{i,j} = \frac{1}{\Delta x^2}(\eta_{i-1,j} + \eta_{i+1,j} + \eta_{i,j-1} + \eta_{i,j+1} - 4\eta_{i,j})$$

where the parameter η could be either the fields μ or φ and spatial distance $i - (i + 1) = j - (j + 1) \rightarrow \Delta x$.

Since the governing equations (4.18), (4.29b), (4.36b) for the phase evolution are non-linear, a parabolic approximation is assumed for each equation respectively:

$$\epsilon^2 \dot{\varphi} = -f'(\varphi) \epsilon^{-1} + \frac{K_n}{2} \rho^2 + K_f(\varphi) (\rho - 1/2) + \epsilon \gamma \Delta \varphi \quad (4.37)$$

$$\epsilon^2 \dot{\varphi} = -f'(\varphi) \epsilon^{-1} + K_n \frac{\rho^2}{2} + \epsilon \gamma \Delta \varphi \quad (4.38)$$

$$\epsilon^2 \dot{\varphi} = -f'(\varphi) \epsilon^{-1} - \frac{1}{2} + \rho + \epsilon \gamma \Delta \varphi. \quad (4.39)$$

in which if ϵ is small enough, then the governing equations hold true ($\epsilon^2 \approx 0$). The evolution of the system is implemented by approximating the time derivatives of phase and concentration as $(\dot{\varphi} \simeq (\varphi_{i,j}^{m+1} - \varphi_{i,j}^m) / \Delta t)$ and $(\dot{\rho} \simeq (\rho_{i,j}^{m+1} - \rho_{i,j}^m) / \Delta t)$ where m and $m + 1$ are incremental time steps of duration Δt .

4.1.2 Gauss-Seidel Algorithm

The most accurate method of solving equations (4.29) or (4.36) in a numerical routine, subject to stability constraints, is a finite difference approach. The equations are discretized in an implicit scheme where the gradient terms are replaced by second order, 5 term Laplacians. Two dimensional square matrices are created for both solute concentration and phase-fields, with i and j as index counters in increments of Δx ; m is chosen as the counter for each time step of duration Δt . This scheme is shown for the case of grain coarsening.

$$\rho_{i,j}^{m+1} = M \frac{\Delta t}{\Delta x^2} (\mu_{i-1,j}^m + \mu_{i+1,j}^m + \mu_{i,j-1}^m + \mu_{i,j+1}^m - 4\mu_{i,j}^m) + \rho_{i,j}^m \quad (4.40a)$$

$$\mu_{\square}^m = [1 + (1 - \varphi_{\square}^m) K_n] \rho_{\square}^m. \quad (4.40b)$$

$$0 = -\epsilon_{i,j}^{-1} \varphi^{m+1} (1 - \varphi_{i,j}^{m+1}) (1 - 2\varphi_{i,j}^{m+1}) - \frac{(\rho_{i,j}^{m+1})^2}{2} + \epsilon \gamma \Delta \varphi_{i,j}^{m+1} \quad (4.41a)$$

$$\Delta \varphi_{i,j}^{m+1} = \frac{1}{\Delta x^2} (\varphi_{i-1,j}^{m+1} + \varphi_{i+1,j}^{m+1} + \varphi_{i,j-1}^{m+1} + \varphi_{i,j+1}^{m+1} - 4\varphi_{i,j}^{m+1}) \quad (4.41b)$$

As these two equations are coupled and (4.41) is nonlinear, they must be solved in an iterative Gauss-Seidel scheme. Solving the cubic polynomial (4.41a) for $\varphi_{i,j}^{m+1}$

produces only one real root if

$$\gamma \left(\frac{\epsilon}{h} \right)^2 > 1/2. \quad (4.42)$$

Practically, this limits the developed phase field model to only cases in which the interface energy driving force is greater than the free energy driving force (i.e. in the axisymmetric case, the inner grain can only shrink). The solute diffusion is a straightforward linear equation which is easily solved through discretization. The phase-field evolution is governed by an elliptical equation, and as a consequence of the gradient term $\Delta\varphi$ in (4.29b) the phase-field value at each point in the matrix is sensitive to all neighbors. As with the gradient of chemical potential, the phase-field gradient is found from first nearest neighbors

$$\Delta\varphi_i \rightarrow \frac{(\varphi_{i-1} + \varphi_{i+1} - 2\varphi_i)}{\Delta x^2}. \quad (4.43)$$

The third order equation resulting from the combination of (4.18), (4.20), and (4.43) must be solved simultaneously for all points in the matrix. This task is accomplished through a Gauss-Siedel routine. The governing equation is regrouped according to

powers of φ :

$$\begin{aligned}
0 &= a \varphi_i^3 + b \varphi_i^2 + c \varphi_i + d \rho_i^2 + e (\varphi_{i-1} + \varphi_{i+1}) & (4.44) \\
a &= -4\epsilon^{-2}; b = 6\epsilon^{-2}; c = -2\epsilon^{-2} - 2\frac{\gamma}{\Delta x^2}; \\
d &= -\frac{1}{2}\epsilon^{-1}; e = \frac{\gamma}{\Delta x^2}.
\end{aligned}$$

Of the three solutions to φ_i in equation (4.44), only one is real and positive.

Again terms are grouped to reduce clutter:

$$\begin{aligned}
\varphi_i &= \frac{1}{3\sqrt[3]{2a}} \left(C_{combo} - \sqrt[3]{2b} + C_1 C_{combo}^{-1} \right) & (4.45) \\
C_1 &= 2^{2/3}(b^2 - 3 a c); \\
C_2 &= 2 b^3 - 9 a b c + 27 a^2 [d \rho_i^2 + (\varphi_{i-1} + \varphi_{i+1})]; \\
C_{combo} &= \left(\sqrt{C_2^2 - C_1^3 - C_2} \right)^{1/3}.
\end{aligned}$$

In the Gauss-Seidel scheme, each time step involves enough pseudo-time steps (denoted by the counter k) for the phase-field to relax to steady state while the concentration profile is frozen ($\rho_i \rightarrow \rho_i^m$). At each time pseudo-time step each point in the phase-field matrix is registered in turn solving (4.45) while the phase-field values of neighbors are fixed ($\varphi_i \rightarrow \varphi_i^{m,k+1}$ and $\varphi_{i\pm 1} \rightarrow \varphi_{i\pm 1}^{m,k}$). The maximum value of k is chosen such that the change in phase field values from one pseudo-time step to the

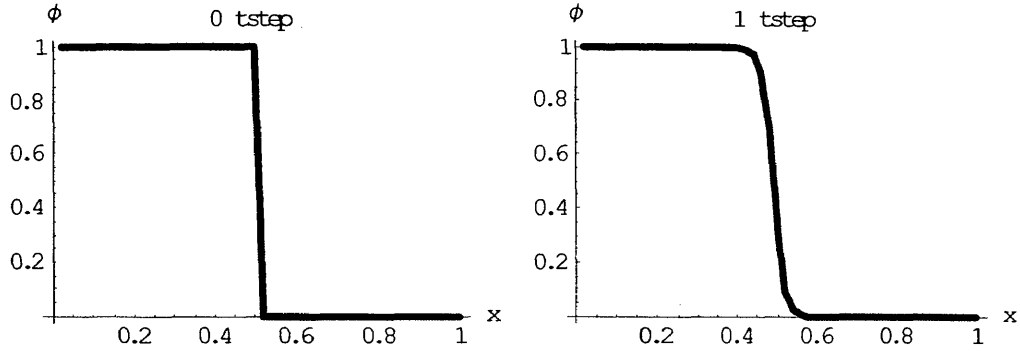


Figure 4.2: Relaxation of phase-field from sharp-interface initial condition after 10 pseudo-time steps. There is no driving force on the boundary ($\rho_i = 1$, $\epsilon = 0.1$, $\Delta x = 0.02$).

next is negligible ($k = k_{\max}$ when $\varphi_i^{m,k+1} - \varphi_i^{m,k} \cong 0$). When the pseudo-time loop ends, the phase-field changes are registered ($\varphi_i^{m,k_{\max}} \rightarrow \varphi_i^{m+1}$), the boundaries of the concentration field and phase field are updated according to Neumann conditions, and the real time counter steps. Figure 4.2 shows how an imposed sharp-interface initial phase-field condition naturally relaxes to a smooth continuum interface.

CHAPTER 5

DIGITAL KINETICS MODEL

The digital kinetics model relies solely on Monte Carlo sampling to implement diffusional and microcrystalline changes without the limitation of maintaining continuity throughout the system. Kinetics are governed by jump statistics instead of field equations such as Fick's second law. Driving forces including chemical potential gradients, grain boundary energy, and body forces factor into the jump statistics of the Potts model. Monte Carlo mechanisms are employed to model both solute diffusion and phase boundary motion.

Solute diffusion is treated as pseudo-atomistic. The concentration is discretized into small steps and each site in the lattice contains quanta of concentration steps, $\Delta\rho$. These finite bits of mass jump from site to site according to driving forces and thermally activated random walk. This differs from traditional atomistic models in that the scale is larger and each point in the lattice represents a discrete volume rather than a single crystal lattice site.

The Potts model is used to simulate microstructure evolution in the digital kinetics scheme. The phase lattice array carries integer values for the phase parameter. The integer phase parameter represents a particular chemical phase and/or a discretized orientation. A two grain system would have two phase values. The special case of the two-phase Potts model is more often referred to as the Ising model. In the Ising model the two phases are represented by two possible spin states $s = \pm 1$. For stable phases, the system minimizes the energy by grouping sites of the same spin state together. Grain boundaries are then infinitesimal lines between sites of different spins. The sharp interface Potts model is shown to accurately predict grain boundary dynamics down to a ratio of boundary width to grain diameter value of 2.5×10^{-3} .

For each time step, the concentration field is first fully updated with changes determined from the atomistic diffusion routine and then the phase field is progressed through the Potts model routine. Zero mass flux (Neumann) conditions are applied at the boundaries for the concentration field. The routines are derived here on a one dimensional lattice indexed by i . The concentration at points throughout the lattice store as ρ_i while the Ising spin-states (phase) are denoted as φ_i . Adding more dimensions simply increases the number of nearest neighbors with which each

site interacts. Non-cubic lattices can be accommodated by considering next-nearest neighbor interactions that are weighted by the increased interaction distance.

5.1 Digital Kinetics Diffusion

Though a finite difference implementation of Fick's second law is simple and effective, the confidence in this bulk-derived law is suspect at a sharp grain boundary. An atomistic model for diffusion is adapted in which solute atoms transfer from site to site based on boltzmann statistics. Since the scale of our target model is meso-scopic, tracking the movement of individual atoms would be highly inefficient. Instead the digital kinetics scheme scales the atomic lattice points up to finite elements of mass on the sub-grain scale and applies the same mechanics. Quanta of solute concentration jump through the lattice in a quest for an energetically minimal resting place. An energetically favorable exchange produces a statistically greater chance of succeeding, though according to thermally driven entropy, energetically unfavorable exchanges are allowed. It should be noted that one consequence of adapting an atomistic model to a scale it was not intended for is that the temperature term in the boltzmann probability becomes non-physical and calibration is required.

Monte Carlo sampling is employed wholesale throughout the modeling routine.

The sampling site is chosen randomly with equal weight applied to all sites inside the system boundaries. In order to eliminate systematic anisotropy, the direction of the concentration jump (whether to or from the sampling site) is chosen randomly ($\Delta\rho_i = \pm|\Delta\rho|$). Next the energy change is calculated for a $\Delta\rho$ exchange with all nearest neighbors. The exchange site is randomly chosen from the neighbors based on probabilities weighted according to the respective energy change values. The exchange is accepted if the driving force calculated from the energy change is sufficient to overcome boltzmann statistics.

The formulation of our pseudo-atomic diffusion begins by assigning a chemical potential relative to the properties of the resident phase A as

$$\mu_A = k_A(\rho - \rho0_A), \tag{5.1}$$

where K_A is the energy gradient coefficient and $\rho0_A$ is the equilibrium concentration for the A phase. Since the digital kinetics system relies upon calculated probabilities, the relationships need not be non-dimensionalized, there is no reason to formulate different expressions for precipitation and grain coarsening and the chemical potential will remain of the same form. The corresponding energy for a site with concentration

ρ_i and phase φ_i follows from the definition of free energy as

$$\varepsilon(\rho_i, \varphi_i) = \frac{k_{\varphi_i}}{2}(\rho_i - \rho_{0\varphi_i})^2 + \varepsilon_{0\varphi_i}. \quad (5.2)$$

The phase dependant bulk energy term $\varepsilon_{0\varphi_i}$ sets a bias for the resident phase.

Once a sampling site i and the sign on $\Delta\rho_i$ are chosen, the system free energy change for an exchange with each neighboring site is calculated (neighbor sites denoted by subscript k) :

$$\Delta\varepsilon_{i,k} = [\varepsilon(\rho_i + \Delta\rho_i, \varphi_i) - \varepsilon(\rho_i, \varphi_i)] + [\varepsilon(\rho_k - \Delta\rho_i, \varphi_i) - \varepsilon(\rho_k, \varphi_i)]. \quad (5.3)$$

The driving force for the exchange is positive if the process results in a net decrease in free energy ($F_k \propto -\Delta\varepsilon_{i,k}$). A concentration exchange to a neighboring site that results in a larger drop in system energy is more likely to be chosen as the target exchange site. In order to properly scale the value of the free energy driving force relative to the thermal energy RT , it is observed from equation (5.2) that the energy gradient constant must have the units [*energy/concentration*²]. Since the chosen unit of measure for concentration is $\Delta\rho$, the scaled driving force must be:

$$F_{i,k} = -\Delta\varepsilon_{i,k}/\Delta\rho^2. \quad (5.4)$$

An Arrhenius-type equation gives the probability of an exchange for each neighbor's driving force. The probabilities of exchange for each neighbor are ratioed to a

total probability of one.

$$\gamma_{i,k} = \exp\left(-\frac{F_{i,k}}{R T}\right). \quad (5.5)$$

$$\gamma_{i,k}^{scaled} = \frac{\gamma_{i,k}}{\sum_k \gamma_{i,k}} \quad (5.6)$$

The exchange site is found from the Monte Carlo sampling between the scaled probabilities. Whichever neighbor site is chosen is put to the final acceptance test. In a true atomistic model, the jump probability would be scaled with the lattice vibration frequency and lattice spacing. In the digital kinetics scheme the exchange probability is scaled with the system scaling factor λ , which plays the same role as the scaling term ν used by Mendeleev and Srolovitz [48]. A sample probability γ_{rand} between zero and one is chosen at random and compared to our calculated probability to determine if the exchange is accepted.

$$\lambda \gamma_{i,k} + \gamma_{rand} \begin{cases} < 1 & ; \text{ exchange rejected} \\ \geq 1 & ; \text{ exchange accepted} \end{cases} \quad (5.7)$$

It becomes clear from equation (5.5) that an increase in energy lowers the probability of an exchange. A high activation energy makes all exchanges less probable while a high thermal energy allows for a higher frequency of energetically unfavorable

exchanges. Since there is no inherent time scale in any of the constant terms, the mobility must either be carefully calculated or else calibrated.

5.1.1 Grain Boundary Effects on Diffusion

The unique properties of the sharp grain boundary are the motivation for adopting an atomistic approach to modeling diffusion. These special properties are introduced at the lattice sites bordering a phase boundary. It is assumed that within the boundary width and within a narrow layer of the grain surfaces, the equilibrium concentration of solute reaches unity [25] and the mobility is increased by an order of magnitude [51].

The grain boundary could be treated as a separate phase but this has two major drawbacks. By assigning a point in the lattice to the boundary, this balloons the width of the boundary up to the lattice spacing, eliminating the sharp interface feature of the model. Also since diffusional exchanges only occur between nearest-neighbors, a separate phase in the boundary would buffer interaction between two grains. To dodge these two problems, the grain boundaries of our system will be reduced to an infinitely sharp line located between two lattice points of different phase assignments. It is assumed that the unique properties of the grain boundary will be extended into

the surface layer of each grain. Thus, 'enhancements' are assigned to the properties of any site located next to a boundary. To these grain boundary (GB) sites, the following modifications apply:

$$\mu_{i,GB} = k_{\phi_i}(\rho_i - 1) \quad (5.8)$$

$$\Delta\rho_{i,GB} = \pm 10 \cdot |\Delta\rho|. \quad (5.9)$$

The dramatic increase of solute diffusion rate in a grain boundary is due to a much lower activation energy. However it is desired to keep the scale of the probability of an energetically-favorable jump on the order of unity in the interests of model efficiency. The increased diffusion rate is more efficiently accommodated by increasing the amount of solute exchanged than by increasing the scaling on exchange probability. The more arduous method would involve assigning a larger activation energy to sites neighboring a boundary, and adjusting the time scaling such the probability of an energetically-favorable jump *in the grain boundary* is on the order of unity. Such scaling would mean that many time steps would need to occur before an energetically-favorable jump in a bulk grain was allowed.

5.2 Microstructural Evolution

The microstructural evolution of the system is handled by much the same method as the solute diffusion. A trial is performed in which a chosen site considers changing phase. Monte Carlo sampling is employed to choose a target site i from all sites within the system boundary. Unlike the diffusion scheme, phase values are not exchanged and phase parameters are not conserved. Phase transitions are driven by the minimization of Gibbs energy balanced with the minimization of the surface energy. A site that matches spin with the majority of its neighbors and have a minimal energy will be the most statistically stable. A system with a higher thermal energy tolerates more energetically unfavorable phase sites. If the driving forces are sufficient to cause a site to switch spin state, this shifts the position of the grain boundary line. The transition of a site from one phase to another must follow the following three axioms:

Axiom 1 *Local equilibrium: The chemical potential at a site must remain constant in the course of switching phase. The transition from one free energy curve to another must occur along the constant-potential energy tie line according to the Onsager relationship.*

Axiom 2 *Conservation of mass: The sum of concentration values in the system as a whole must remain constant during a transition.*

Axiom 3 *Common tangent construction: The Onsager relationship gives the driving force for a phase transition according to a common tangent line between two free energy curves.*

Driving forces for phase transitions are calculated from the change in free energy and change in interface energy ($A\gamma$).

$$F_i^{trial} = -\Delta (b s_i - E(\rho_i^{init}, s_i) + \mu_i \rho_i^{init}). \quad (5.10)$$

The body force constant b sets a bias for one phase; s_i is the initial spin state. The chemical potential μ keeps the same form as (5.1) and the form of the internal energy $E(\rho_i)$ is the same as in equation (5.2). In switching spin state ($s_i^{trial} = -s_i^{init}$), the concentration of the target site must shift in order to obey the local equilibrium assumption as stated in axiom 1:

$$\mu_i^{trial} = \mu_i^{init} \quad (5.11a)$$

$$K_{-s_i}(\rho_i^{trial} - \rho_{0-s_i}) = K_{s_i}(\rho_i^{init} - \rho_{0s_i}) \quad (5.11b)$$

$$\rho_i^{trial} = \frac{K_{s_i}}{K_{-s_i}}(\rho_i^{init} - \rho_{0s_i}) + \rho_{0-s_i}. \quad (5.11c)$$

If the concentration of the of the target site changes by $\rho_i^{trial} - \rho_i^{init}$, the summed concentration of the rest of the system must adjust by this amount in accordance to axiom 2. The contribution is assumed to come from all the immediate neighbors according to their relative chemical potential values.

$$\sum_k^{neighbors} (\rho_k^{trial} - \rho_k^{init}) = -(\rho_i^{trial} - \rho_i^{init}) \quad (5.12)$$

$$\rho_k^{trial} = \rho_k^{init} - \frac{\mu_k}{\sum_k \mu_k} (\rho_i^{trial} - \rho_i^{init}) \quad (5.13)$$

The driving force F_i^{trial} is calculated for the target site based on the new concentration value and new phase according to axiom 3. The driving force contribution for each of the neighbors, F_k^{trial} , is calculated from the new concentration values and the average chemical potential values during the trial. The sum of these all these driving forces, $F_{i,net}^{trial}$, makes up the chemical contribution to the total driving force.

$$F_i^{trial} = -2b s_i - [E(\rho_i^{trial}, -s_i) - E(\rho_i^{init}, s_i)] + \mu_i (\rho_i^{trial} - \rho_i^{init}) \quad (5.14)$$

$$F_k^{trial} = - [E(\rho_k^{trial}, s_k) - E(\rho_k^{init}, s_k)] + \frac{\mu_k^{trial} + \mu_k^{init}}{2} (\rho_k^{trial} - \rho_k^{init}) \quad (5.15)$$

$$F_{i,net}^{trial} = F_i^{trial} + \sum_k^{neighbors} F_k^{trial} \quad (5.16)$$

The interface energy is calculated over all nearest neighbors (indexed by k) and scaled with the constant areal grain boundary energy term J . For a two-phase system the interface energy at a site i can be found from the number of like-spin neighbors

(5.17). If next nearest neighbors are considered, or if a non-cubic lattice is modeled, the relative contribution to the boundary energy from each neighbor can be scaled by the factor wt_k . The difference in interface energy from the initial state to the trial state is combined with the chemical driving force (5.16) to find the total driving force of the trial, $F_{i,total}^{trial}$:

$$spinsum_i = \sum_k^{neighbors} \frac{J}{2} \cdot s_i \cdot s_k \cdot wt_k \quad (5.17)$$

$$F_{i,total}^{trial} = - (F_{i,net}^{trial} - (spinsum_i^{trial} - spinsum_i^{init})) / \Delta\rho^2. \quad (5.18)$$

The driving force for phase-switching is utilized in a similar way as in the diffusion scheme (5.5). If the driving force is positive or if the probability is large enough compared to a randomly generated sample probability γ_{rand} , the phase-switch passes the first trial. The overall rate of grain boundary migration is scaled by a final trial of comparing a migration mobility M_{mig} to another sample probability.

$$\left. \begin{array}{l} F_i^{trial} \geq 0 \quad \text{OR} \\ \exp\left(\frac{F_i^{trial}}{R T}\right) + \gamma_{rand} \geq 1 \end{array} \right\} \text{trial continued} \quad (5.19a)$$

$$M_{mig} \geq \gamma_{rand} \quad ; \quad \text{phase change accepted} \quad (5.19b)$$

$$M_{mig} < \gamma_{rand} \quad ; \quad \text{phase change rejected}$$

CHAPTER 6

RESULTS

Thesis Question: Is it possible to construct a discrete, probabilistic simulation of grain and precipitate boundary evolution in the presence of a diffusing solute?

Answer: Yes.

The objective of this thesis was to present the digital kinetics model for simulating precipitation and grain coarsening. Preliminary validation of the model against the predictions of the sharp-interface theory and results from the phase-field numerical model are shown here.

The phase-field and sharp-interface models were adapted for the systems of interest. The finite difference version of Fick's law of diffusion in the phase-field model was compared directly to the pseudo-atomistic diffusion scheme of the digital kinetics model. The phase-field model and the digital kinetics model were both implemented under conditions that could be compared to predictions from the sharp-interface the-

ory. The test system selected is a two-dimensional, two-phase system in which a smaller circular grain is set inside a parent matrix. The system domain is of dimensions $2\pi \times 2\pi$ and the inner grain is introduced with an initial radius of $0.2 \times 2\pi$.

Since the continuous phase restriction of the phase-field model cannot handle the large incongruities of fast diffusion in a grain boundary, the special grain boundary rules of the digital kinetics model will not be used. The random nucleation of grains will be discouraged by using a high boundary energy term and neither phase will be given a preferential bias. The following set of conditions are used in the digital kinetics model while comparing to the phase-field model:

- grain boundary potential, $\mu_{i,GB} \equiv \mu_{i,bulk}$
- grain boundary concentration scaling, $\Delta\rho_{i,GB} = \pm |\Delta\rho|$
- phase bias, $b = 0$

6.1 Diffusion Check

The digital kinetics diffusion scheme is first tested against the numerical solution of Fick's law from the phase-field model. Both grains are assigned the same phase parameters $K_m = K_p = 1.0$ and $\rho_0_m = \rho_0_p = 0.0$. Zero-flux conditions are applied

to the boundaries. Figure 6.1 shows a cross section of both digital kinetics and phase-field solutions with the following run conditions:

Phase-field parameters: 1000 grid points, $M = 2.0$, $\Delta x = 2\pi \times 10^{-2}$, $\Delta t = 10^{-4}$, *steps* = 2500

Digital kinetics parameters: 1000 grid points, $\lambda = 0.08$, $\Delta \rho = 0.01$, *steps* = 500

Different sets of parameters can produce concentration profiles that do not match Fick's law, though the same steady state profile is reached in the end. Figure 6.2 shows two different runs that are characterized as "square" and "straight". These results are discussed in the next chapter.

6.2 Precipitation

A direct comparison of the sharp-interface, phase-field, and digital kinetics models would, ideally, compare interface position and field values at several time steps during a precipitation event. This is quite difficult to accomplish for the sharp-interface model though because jump conditions must be satisfied across a moving interface. In fact, it is just this difficulty that has motivated the development of regularized algorithms like the phase-field paradigm. In light of this, a preliminary comparison

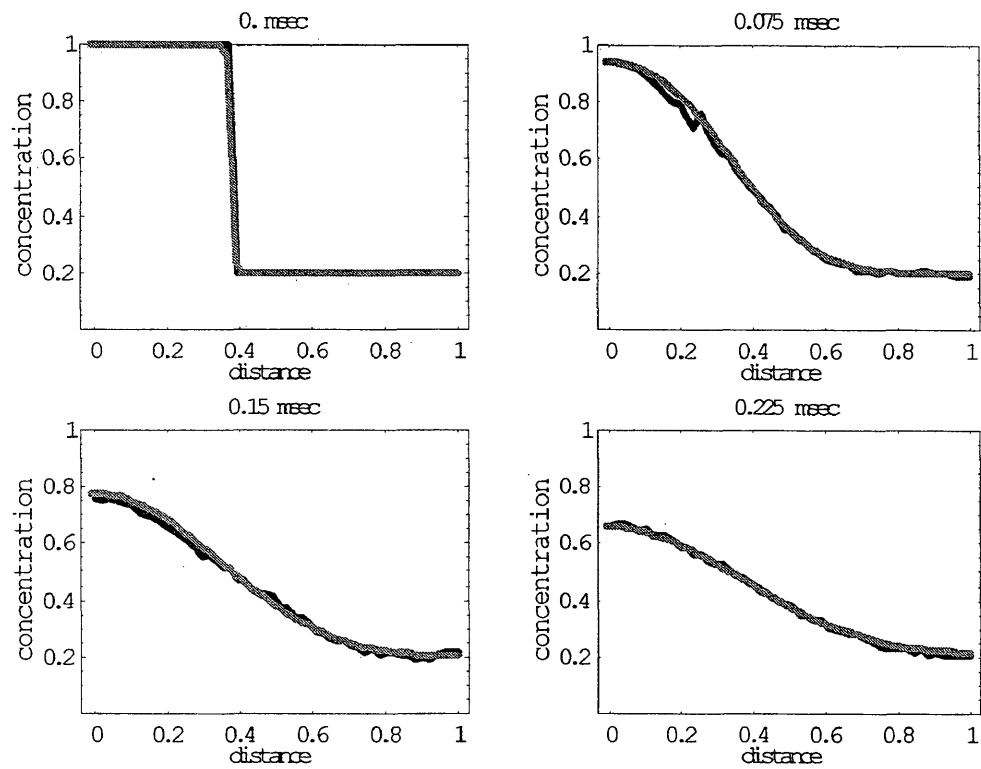


Figure 6.1: Concentration profile solutions to diffusion in 2-D lattice. The lighter line is the phase-field solution, darker, uneven line is the digital kinetics solution.

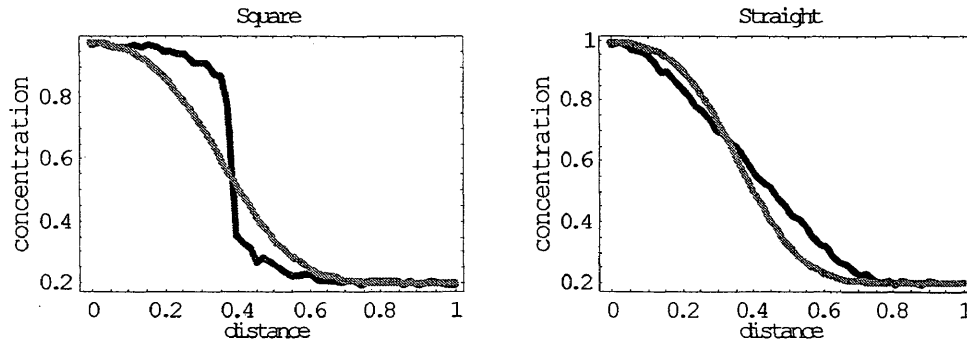


Figure 6.2: Examples of digital kinetics simulations with unstable parameters. Left: $\Delta\rho = 0.005$, $M_{DK} = 5.0$; Right: $\Delta\rho = 0.01$, $M_{DK} = 0.005$.

was made wherein a precipitate was allowed to grow to until the matrix solute was exhausted and a steady state size was achieved. This size, derived for phase-field and digital kinetics models, can be compared with the area fraction prediction of the sharp-interface theory. Initial conditions of $\rho_{init}^+ = 0.2$, $\rho_{init}^- = 1.0$, $s_{init} = 0.2*2\pi$, $R = \pi$, $\sigma = \frac{1}{6}$ are applied to equation (3.18). The resulting prediction for the equilibrium area fraction is 0.193.

The phase-field model was run with surface free energy $\gamma = 6\sigma$ from (4.21). Figure 6.3 shows the evolution of the fractional precipitate area and Figure 6.4 shows the concentration at several time steps using the same initial conditions as above for the sharp-interface result and the following conditions:

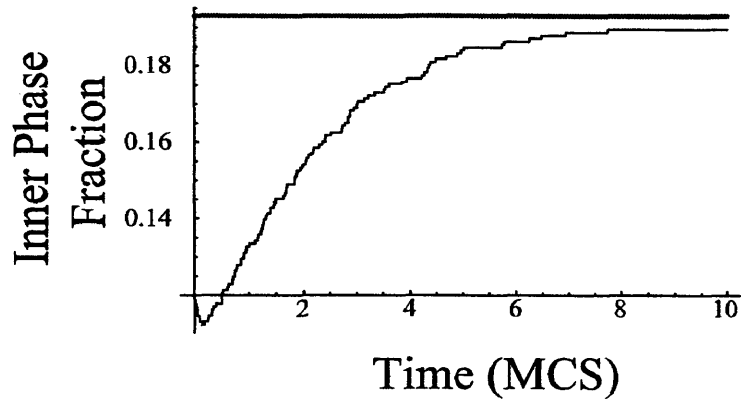


Figure 6.3: Solution to the evolution of the fractional precipitate area from the phase-field model. The straight line shown is at the sharp-interface prediction of 0.193.

Phase-field parameters: 1000 grid points, $\epsilon = 0.1$, $\gamma = 1.0$, $M = 2.0$, $\Delta x = 2\pi \times 10^{-2}$, $\Delta t = 10^{-6}$, $steps = 2 \times 10^7$

The digital kinetics model was also run using the same initial conditions to simulate precipitation. However, the parameters used in the Monte Carlo sampling scheme do not correlate to the parameters used in the sharp-interface and phase-field models, because the time and length scales of the model have yet to be matched with those of the sharp-interface theory as was accomplished in the work of Liu and Lusk with elastic effects [2],[3]. It was necessary to search for the equivalent parameters

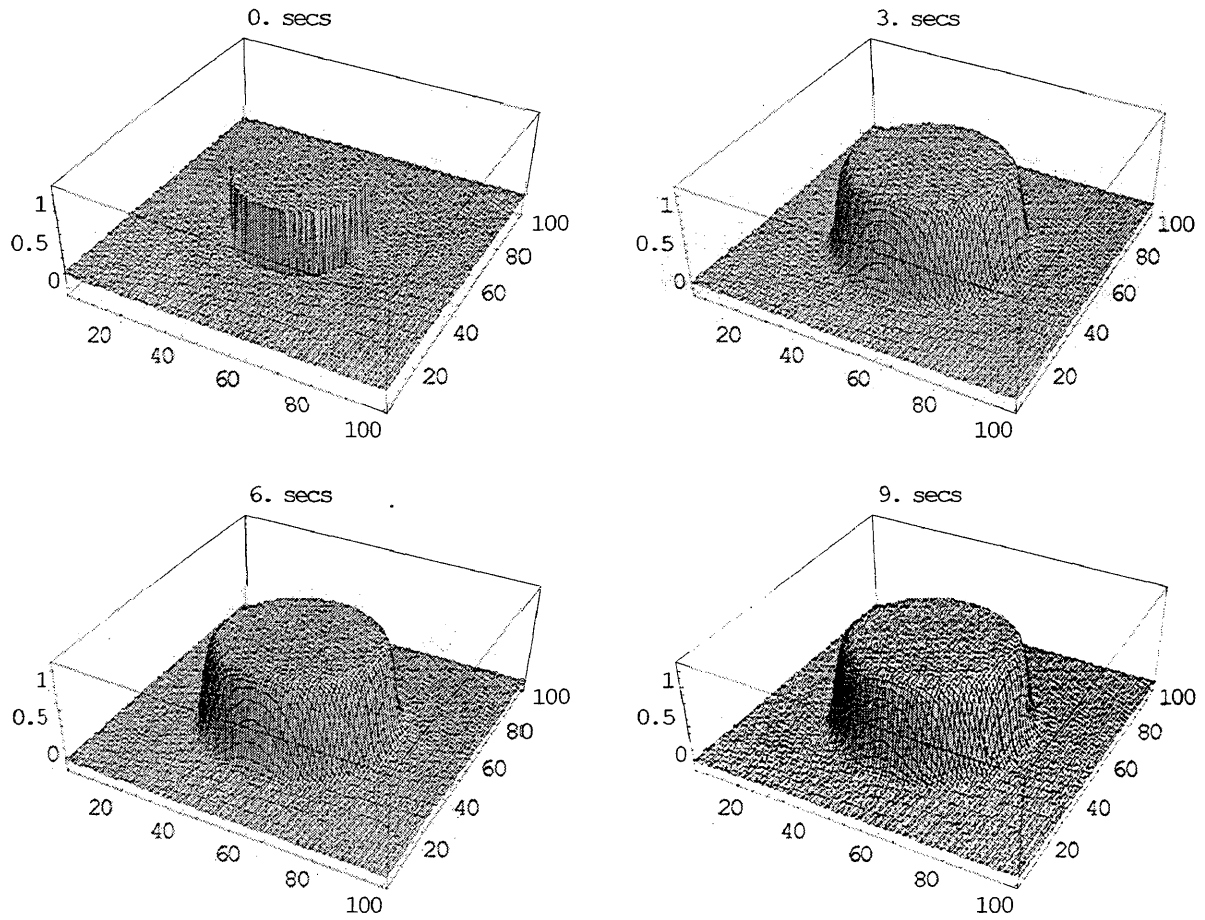


Figure 6.4: Concentration profiles for phase-field precipitation modeling results at various time steps.

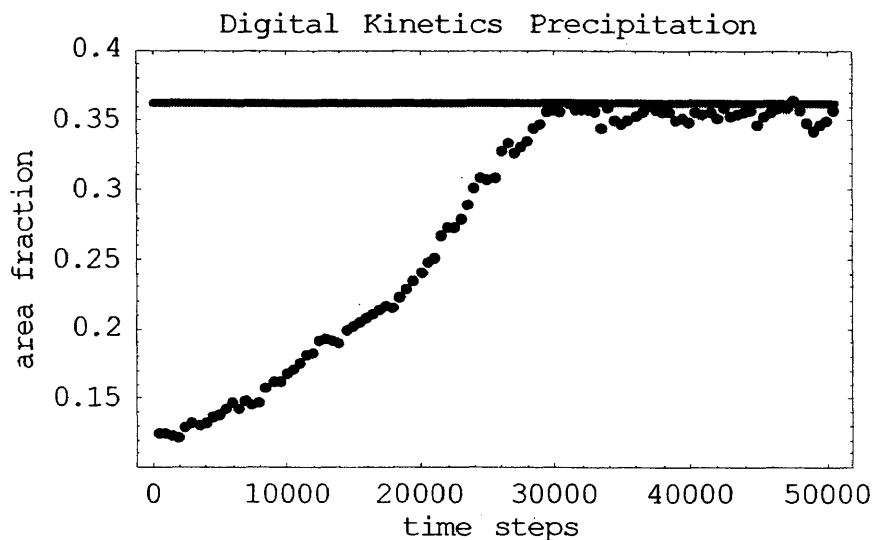


Figure 6.5: Solution to the evolution of the equilibrium precipitate area from the digital kinetics model. The straight line indicates averaged equilibrium precipitate size.

through experimentation. Figure 6.5 shows the evolution of a grain toward an equilibrium grain size while Figure 6.6 shows the concentration at several time steps. The following parameters are used in this model:

Digital kinetics parameters: 1000 grid points, $\rho_0_m = 0.0$, $\rho_0_p = 1.0$, $k_m = k_p = 1.0$, $\lambda = 1.2$, $\Delta\rho = 0.01$, $J = 1.7$, $kT = 1.4$, $M_{mig} = 1.0$, $steps = 5 \times 10^4$

Problems arose from the probabilistic nature of the digital kinetics model that

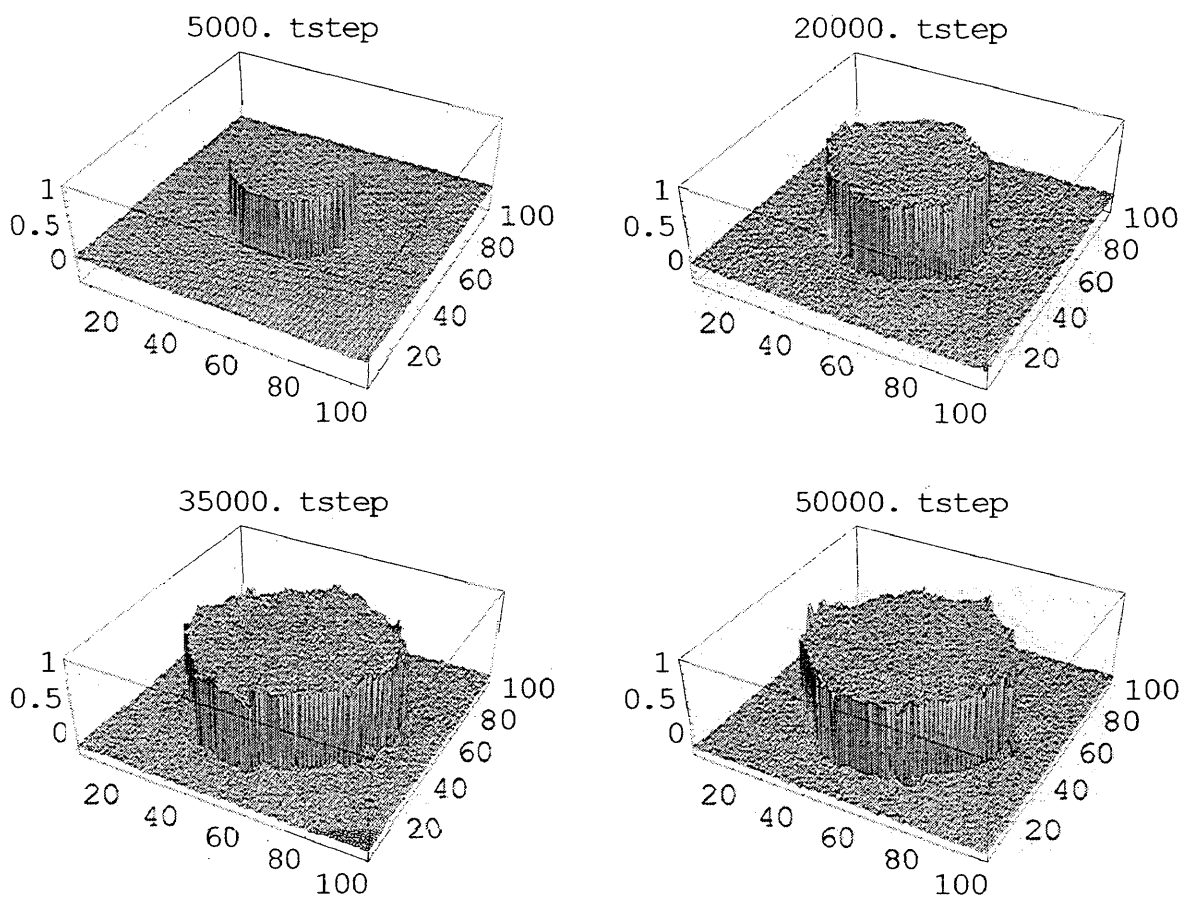


Figure 6.6: Concentration profiles for digital kinetics precipitation modeling results at various time steps.

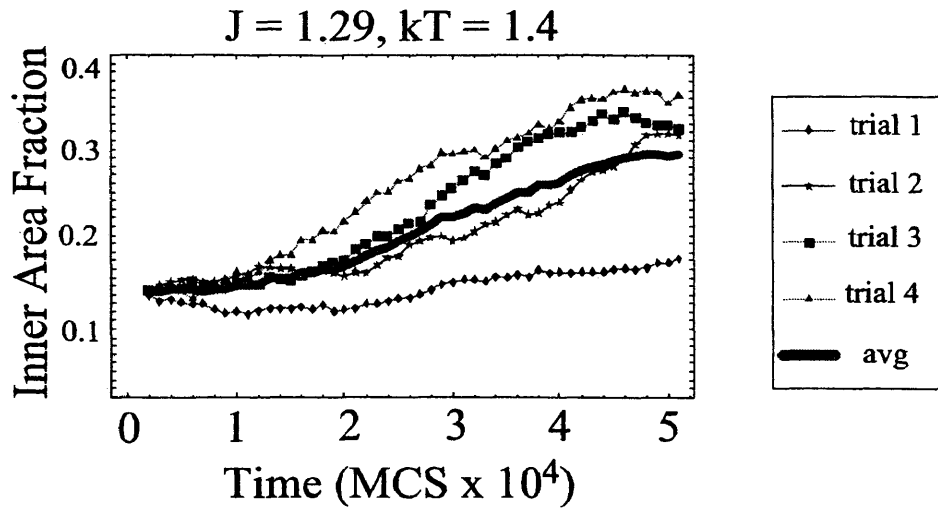


Figure 6.7: Precipitate area fraction solution from four trials of the digital kinetics code using the same parameters but different initial seed.

made experimentation overly time consuming to pinpoint the correct parameters. Figure 6.7 shows the high degree of standard deviation in the digital kinetics results using the same set of conditions yet different random number generator seeds. Even if several such runs are averaged together, as in 6.8, there is uncertainty that the averaged results are representative enough to compare to sharp-interface and phase-field results.

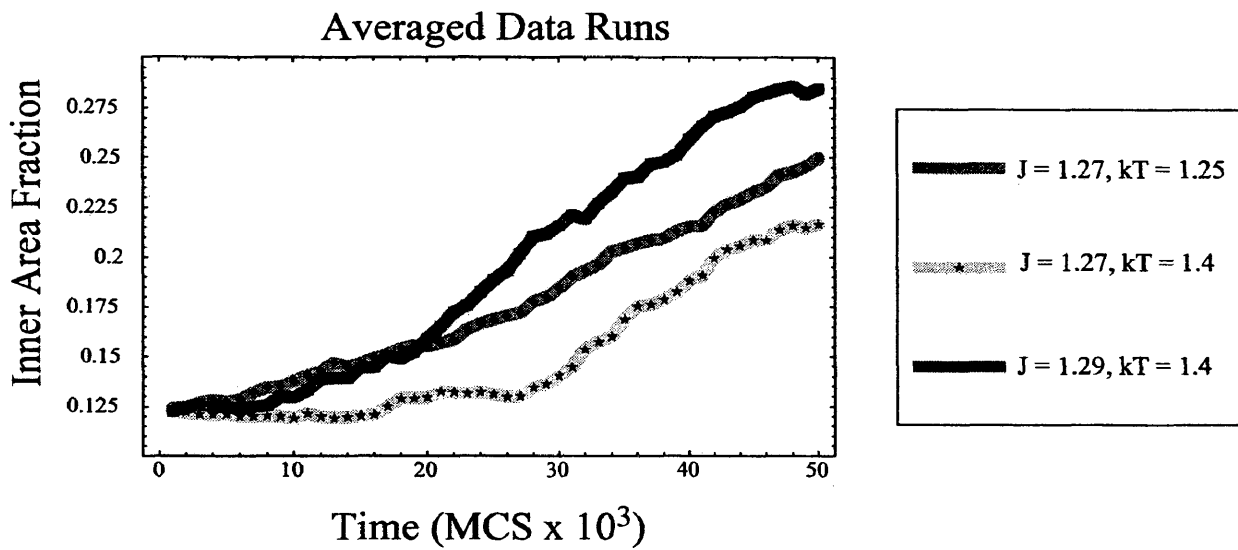


Figure 6.8: Each of the plots represents four trails of the digital kinetics code with different random number generator seeds.

6.3 Grain Coarsening

Since an equilibrium area solution does not exist from the sharp-interface theory for grain coarsening, the three models are compared on the basis of migration rates and concentration profiles. Figure 6.9 shows the close agreement of the sharp-interface theory and the phase field results for various values of K_n . The effects of reducing ϵ , and hence diffuse boundary width, in the phase-field model are demonstrated in Figure 6.10. Equivalent parameters were used for both models.

Figure 6.11 shows cross sections at several time steps for both the phase-field and digital kinetics models. It should be noted that the close match in interface migration rates between the phase-field and digital kinetics models does not imply that the time scaling has been accurately calibrated between the models. The following parameters were used to obtain the results of Figure 6.11:

Phase-field parameters: 1000 grid points, $\epsilon = 0.1$, $\gamma = 1.0$, $K_n = 1.0$, $M = 2.0$, $\Delta x = 2\pi \times 10^{-2}$, $\Delta t = 10^{-4}$, $steps = 15000$

Digital kinetics parameters: 1000 grid points, $\rho_0^m = \rho_0^p = 0.0$, $k_m = 2.0$, $k_p = 1.0$, $\lambda = 1.2$, $\Delta\rho = 0.01$, $J = 1.0$, $kT = 1.0$, $M_{mig} = 0.05$, $steps = 4000$

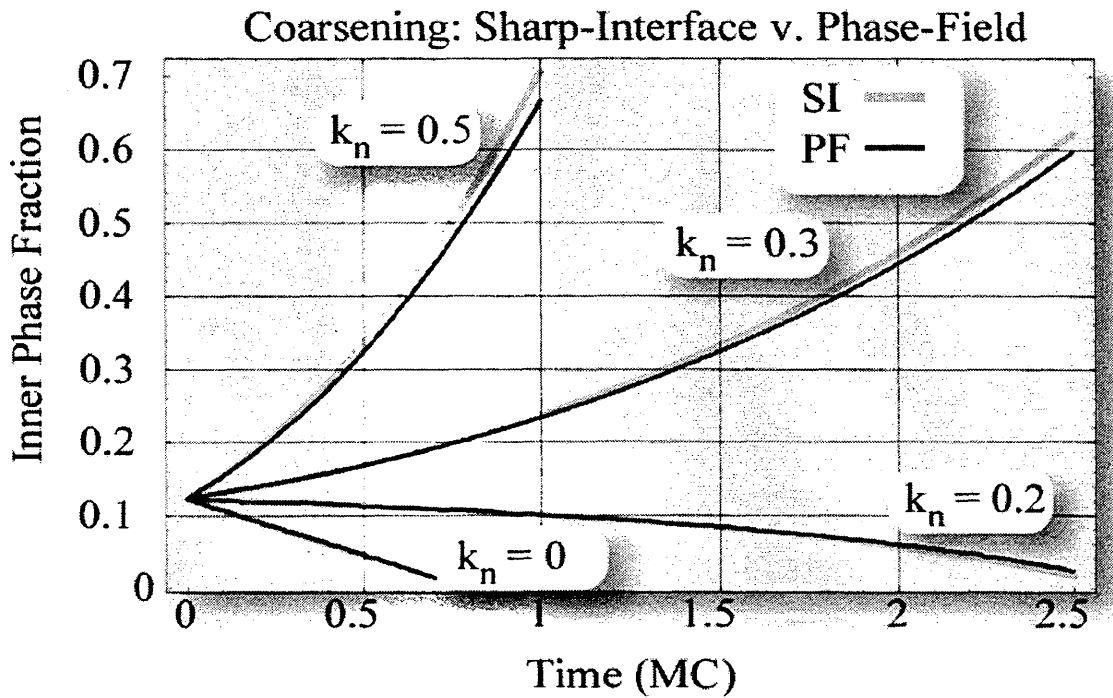


Figure 6.9: Results of coarsening runs in the sharp-interface and phase-field models for different values of K_n .

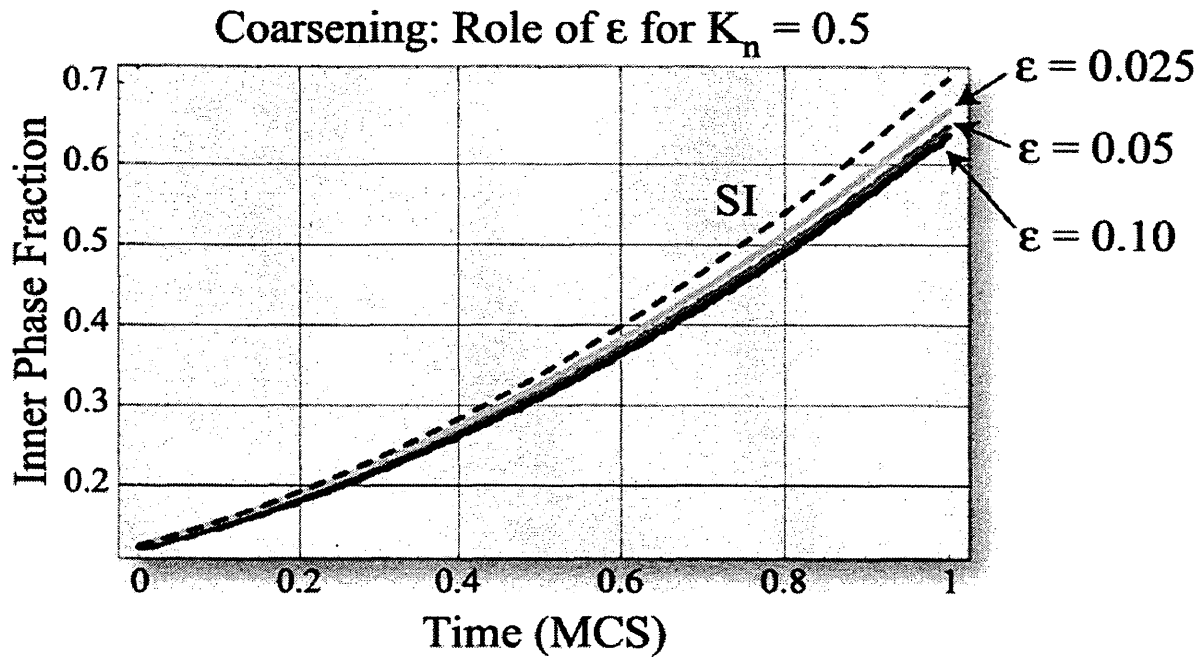


Figure 6.10: Comparison of sharp-interface results (dashed) with phase-field runs using decreasing boundary width. 1000 grid points used for $\epsilon = 0.10, 0.05$; 4000 grid points used for $\epsilon = 0.025$.

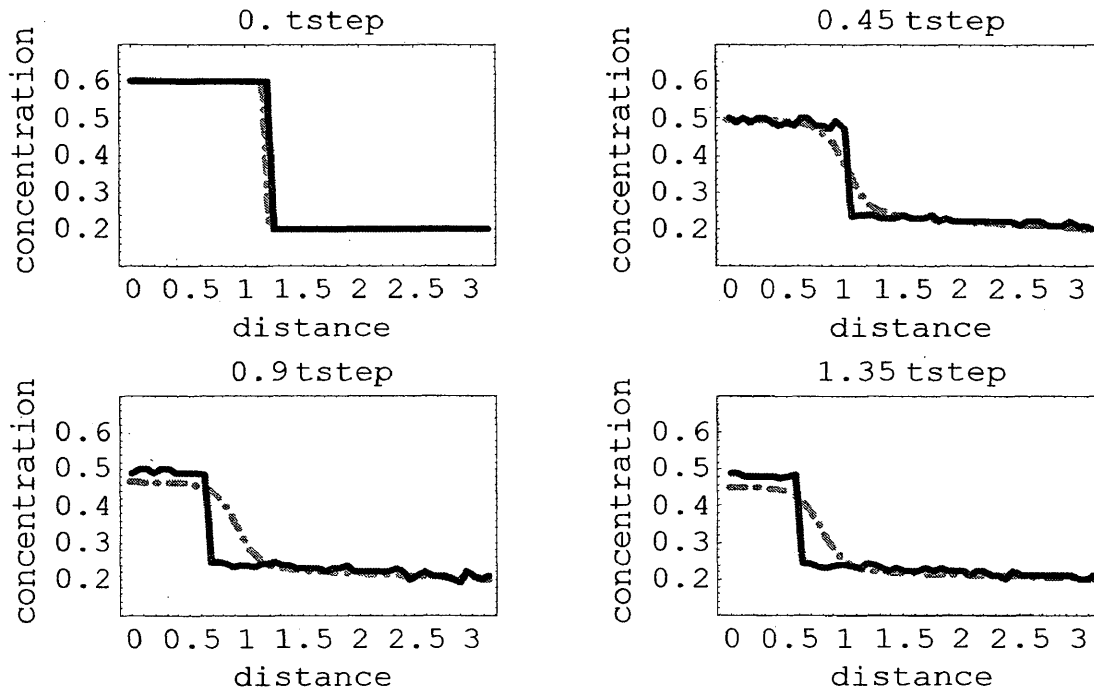


Figure 6.11: Cross sectional profile of grain growth solutions. The dash-dotted line is phase-field solution while the solid line is the digital kinetics. The time scale comes from the phase-field model.

CHAPTER 7

DISCUSSION

This thesis investigation has established that it is possible to create a discrete, probabilistic model for microstructural evolution in the presence of a diffusing solute, and some preliminary validation has been performed. The results of the previous chapter showed the comparisons of the digital kinetics model to solutions from the phase-field model and the predictions of the sharp-interface theory.

The sharp-interface model was adapted to the phenomena of precipitation and grain coarsening with non-dimensionalized equations in an axisymmetric system. A prediction of the fractional equilibrium area for specific precipitation and grain growth systems were obtained from these equations.

The phase-field model was developed from the principles of the sharp-interface theory and adapted for simulating precipitation and grain coarsening. The results of simulating precipitation and coarsening with the two deterministic models are in near agreement. Slight deviations of the phase-field results from the sharp-interface

are a consequence of the diffuse boundary description in the phase-field model.

The digital kinetics model was derived from probabilistic principles based on driving forces and implemented with Monte Carlo sampling routines. The pseudo-atomistic diffusion scheme is shown to match well to Fick's law though it was discovered that the model parameters must fall within the stability requirements as discussed below. The microstructural evolution in the digital kinetics models demonstrates principles similar to the phase-field model, though as a non-deterministic model, direct comparison must be done with time averaged results. As with the phase-field grain coarsening model, the digital kinetics results do not match those of the sharp interface theory, though they closely resemble the phase-field results.

Some discoveries that were made through the course of this research are discussed in greater detail below:

7.1 Diffusion

- *A stability region exists for the diffusion parameters used in the digital kinetics model*

The pseudo-atomistic approach to modeling diffusion is potentially problematic as it attempts to implement a microscopic process on the meso-scale. However, the

successful comparison to the phase-field model proves its worth. The rate agreement in figure 6.1 implies that the digital kinetics time scaling for that set of conditions is $\Delta t = 5 \times 10^{-4}$. However it is necessary to note that in the process of matching the digital kinetics solution to the Fick's law, a range of stability for the parameters was found. When the ratio probability scaling factor λ and the discretized concentration $\Delta\rho$ is within the range $1 < \lambda/\Delta\rho < 100$, the digital kinetics model matches up well as in figure 6.1. If the ratio is below 1 or above the value of 100, the evolving profile is uneven when compared to Fick's law as seen in figure 6.2. This instability is due to unequal weighting to the driving force from either the chemical potential or the gradient of the chemical potential. Within this range of stability, the digital kinetics diffusion scheme is proven to simulate bulk solute diffusion correctly.

7.2 Precipitation

- *The solute profiles for the phase-field and digital kinetics precipitate simulations highlights the features of each model*

Figures 6.4 and 6.6 demonstrate the features inherent in both the phase-field and digital kinetics models. While the interface of the precipitate is smooth and diffuse in the phase-field results, the digital kinetics model produces a more physically realized

concentration profile. Moreover, while the precipitate in the phase-field model grows as a whole, the precipitate of the digital kinetics model grows independently at all points along the interface. The digital kinetics model successfully simulates the features of sharp-interfaces and probabilistic kinetics that are desired.

- *Matching the sharp-interface prediction for equilibrium precipitate size*

The results of figure 6.3 for the phase-field model agree well with the predictions of the sharp interface theory. However, the equilibrium area stops just short of the target value of 0.193. Several differences in the implementation of the models affect this discrepancy. Even though zero-flux conditions are enforced at the boundaries, the finite difference version of the diffusion equation does not guarantee conservation of mass. Small variations in the system mass were observed. Additionally, the sharp-interface result is derived for a system in cylindrical coordinates. While the square system of the phase-field and digital kinetics numerical codes are nearly equivalent to the axisymmetric system of the sharp-interface model grains far from the boundary, there are still some corner effects that could contribute to deviations between model results. Finally, as the asymptotic analysis of Appendix A shows, the phase-field relationships are equivalent to those in the sharp-interface theory only as the boundary width approaches zero ($\epsilon \rightarrow 0$).

An equivalent agreement in results was not found for precipitation in the digital kinetics model. In the case of figure 6.5 the fractional equilibrium size surpassed the target value of 0.193. The parameters used in the Monte Carlo sampling scheme do not correlate to the parameters used in the sharp-interface and phase-field models because they were not derived from the same configurational force balance. It was necessary to search for equivalent parameters through experimentation. Figure 6.7 shows that a high degree of standard deviation is inherent in the digital kinetics results using the same set of conditions yet different random number generator seeds. Even if several such runs are averaged together, as in 6.8, the standard deviation is enough to leave uncertainty that the averaged results are representative enough to compare to sharp-interface and phase-field results. A large set of simulation results must be averaged together in order to truly compare the digital kinetics model to the phase-field model.

It is possible that a stability condition exists for the microstructural evolution scheme as it does for the diffusion scheme. Finding such a stability region will require further experimentation or a detailed derivation correlating the digital kinetics parameters to those of the sharp-interface and phase-field theory.

7.3 Grain Coarsening

The sharp-interface and phase-field models have been shown to agree closely for varying degrees of energy gradient constants in Figure 6.9. The deviation between these models can be explained by the asymptotic approach of the phase-field model with increasingly sharp boundary widths as seen in Figure 6.10. However, the price of decreasing ϵ is increased computation. The lattice size was increased four-fold in order to maintain stability when ϵ was reduced to a value of 0.025.

The close resemblance of the grain coarsening phase-field and digital kinetics results in Figure 6.11 demonstrate the qualitative agreement of the two numerical models. While a time scaling term could be found from the results of Figure 6.11 to link the two models, declaring the validity of such a term would be premature. Any correlation in the interface migration rates will be effected by the same standard deviation discovered in simulating precipitation.

7.4 Further Research

From the previous discussion, the successes of developing the discrete, probabilistic digital kinetics model need to be built upon to fully validate the model as a predictive tool. In future development of the digital kinetics model the following

studies are proposed:

- Compare results of digital kinetics diffusion in single-grain and multiple-grain settings to numerical results of Fick's law and determine appropriate scaling factors for direct comparison. Calibrate the temperature term in the digital kinetics model to an actual system temperature.
- Obtain run-averaged results from the digital kinetics code to compare against the axisymmetric sharp-interface theory and phase-field model for precipitate growth and grain coarsening.
- Once the terms in the digital kinetics model have been linked to those in the phase-field model, verify that the agreement between the models holds for various system initial conditions.
- Compare the results from the digital kinetics model and the phase-field model in more complex systems.
- Expand the digital kinetics model to handle multiple phases and compare to results from multiphase-field models
- Optimize the digital kinetics scheme for faster computation and compare CPU

time to optimized phase-field models in a complex system

- Correlate digital kinetics parameters to physical properties of an alloy system and compare to experimental results
- Apply to a range of systems: annealing of steel, thin-film depositions, DIM regions in diffusion couples

7.5 Conclusions

A new modeling paradigm, the *digital kinetics* model, was created to simulate diffusion and microstructural evolution in solid alloys. The phenomena of grain coarsening and precipitation were simulated using the digital kinetics model and adapted sharp-interface and phase-field models. The solutions from the digital kinetics model demonstrated that the discrete, probabilistic approach does produce realistic results that can be compared to the predictions of the sharp-interface theory and the phase-field model. The modified-atomistic diffusion scheme used in the digital kinetics model successfully produced solutions matching Fick's law, though a range of stability for the parameters must be observed. Preliminary validation demonstrates the qualitative agreement of the of the phase-field and digital kinetics models, though a

quantitative link between the models requires further experimentation.

BIBLIOGRAPHY

- [1] Porter, D. A. and K. E. Easterling, *Phase Transformations in Metals and Alloys* (Second Edition), Nelson Thornes Ltd, Cheltenham UK (1992).

- [2] Liu, P., *A Hybrid Paradigm for Modeling Microstructural Evolution Under the Influence of Stress*, Doctor of Philosophy form Colorado School of Mines (2002).

- [3] Liu, P. and M. T. Lusk, "Parametric Links Among Monte Carlo, Phase-Field, and Sharp-Interface Models of Interfacial Motion", *Physical Review E* 66 061603 (2003).

- [4] Gottstein, G. and L. S. Shvindlerman, *Grain Boundary Migration in Metals*, CRC Press, Boca Raton, Fla., 1999.

- [5] Fried, E. and M. E. Gurtin, "Coherent Solid-State Phase Transitions with Atomic Diffusion: A Thermomechanical Treatment", *Journal of Statistical Physics*, 95:1361 (1999).

- [6] Reynolds, J. E., B. L. Averbach, and M. Cohen, "Self-Diffusion and Interdiffusion in Gold-Nickel Alloys", *Acta Metallurgica*, 5:29 (1957).

- [7] Heckel, R.W. and M. Balasubramaniam. "The Effects of Heat Treatment and Deformation on the Homogenization of Compacts of Blended Powders", *Metallurgical Transactions*, **2**:379 (1971).
- [8] Lee, C. F., "On the Solution of Concentration Distributions in some Binary Alloy Systems", *Acta Metallurgica*, **19**:415 (1971).
- [9] Weatherly, G. C., and R. B. Nicholson, "An Electron Microscope Investigation of the Interfacial Structure of Semi-coherent Precipitates", *Philosophical Magazine*, **17**:801 (1967).
- [10] Aaron, H. B., and G. R. Kotler, "Second Phase Dissolution", *Metallurgical Transactions*, **2**:393 (1971).
- [11] Laird, C. and H. I. Aaronson, "Mechanisms of Formation of θ and Dissolution of θ' Precipitates in an Al-4% Cu Alloy", *Acta Metallurgica*, **14**:171 (1966).
- [12] Clark, J. B, and A. J. McEvily, "Interaction of Dislocations and Structures in Cyclically Strained Aluminum Alloys", *Acta Metallurgica*, **12**:1359 (1964).
- [13] Rabkin, E., V. N. Semenov and A. Winkler, "Percolation Effects During Interdiffusion in the Cu-NiAl System", *Acta Materialia*, **50**:3227 (2002).
- [14] Fujiwara, K. and Z. Horita, "Measurement of the Intrinsic Diffusion Coefficients of Al and Ni in Ni₃Al using Al/NiAl Diffusion Couples", *Acta Materialia*, **50**:1571 (2002).

- [15] Banerjee, R., X. D. Zhang, S. A. Dregia and H. I. Fraser, "Phase Stability in Al/Ti Multilayers", *Acta Materialia*, **47**:1153 (1999).
- [16] Boyd, J. D. and R. B. Nicholson, "A Calorimetric Determination of Precipitate Interfacial Energies in Two Al-Cu Alloys", *Acta Metallurgica*, **19**:1101 (1971).
- [17] Broeder, F. J., and S. Nakahara, "Diffusion Induced Grain Boundary Migration and Recrystallization in the Cu-Ni System", *Scripta Metallurgica*, **17**:399 (1983).
- [18] Broeder, F. J., "Diffusion-Induced Grain Boundary Migration and Recrystallization, Exemplified by the System Cu-Zn", *Thin Solid Films*, **124**:135 (1985).
- [19] Ma, C. Y., E. Rabkin, W. Gust, and S. E. Hsu, "On the Kinetic Behavior and Driving Force of Diffusion Induced Grain Boundary Migration", *Acta Metallurgica*, **43**:3113 (1995).
- [20] Yamamoto, Y., S. Uemura, and M. Kajihara, "Observations on Diffusion-Induced Recrystallization in Binary Cu/Ni diffusion Couples Annealed at an Intermediate Temperature", *Materials Science and Engineering*, **A312**:176 (2001).
- [21] Aaron, H. B. and H. I. Aaronson, "Growth of Grain Boundary Precipitates in Al 4% Cu by Interfacial Diffusion", *Acta Metallurgica*, **16**:789 (1968).
- [22] Winning, M., G. Gottstein, L. S. Shvindlerman, "On the Mechanisms of Grain Boundary Migration", *Acta Materialia*, **50**:353 (2002).
- [23] Chen, H. and J. F. Morral, "Variation of the Effective Diffusivity in Two-Phase Regions", *Acta Materialia*, **47**:1175 (1999).

- [24] Buscaglia, V. and U. Anselmi-Tamburini, "On the Diffusional Growth of Compounds with Narrow Homogeneity Range in Multiphase Binary Systems", *Acta Materialia*, **50**:525 (2002).
- [25] Mendeleev, M. I. and D. J. Srolovitz, "A Regular Solution Model for Impurity Drag on a Migrating Grain Boundary", *Acta Materialia*, **49**:589 (2001).
- [26] Masumura, R. A., B. B. Rath and C. S. Pande, "Analysis of Cu-Ni diffusion in a Spherical Geometry for Excess Vacancy Production", *Acta Materialia*, **50**:4535 (2002).
- [27] Ma, N., S. A. Dregia and Y. Wang, "Solute Segregation Transition and Drag Force on Grain Boundaries", *Acta Materialia*, **51**:3687 (2003).
- [28] Kirchheim, R. "Grain Coarsening Inhibited by Solute Segregation", *Acta Materialia*, **50**:412 (2002).
- [29] Higginson, R. and P. Bate, "Substructure Drag Effects and Recrystallization Textures in Aluminum", *Acta Materialia*, **47**:1079 (1999).
- [30] Yamamoto, Y. and M. Kajihara, "Quantitative Analysis of Observations of Diffusion Induced Grain Boundary Migration for Random Boundaries in the Cu(Zn) System Using a Driving Force Model", *Acta Materialia*, **47**:1195 (1999).
- [31] Brener, E. A. and D. E. Temkin, "Theory of Diffusion Induced Grain Boundary Migration: Is Mass Transport Along Free Surfaces Important?", *Acta Materialia*, **50**:1707 (2002).

- [32] Swiler, T. P., V. Tikare and E. A. Holm, "Heterogeneous Diffusion Effects in Polycrystalline Microstructures", *Materials Science and Engineering*, **A238**:85 (1997).
- [33] Loginova, I., G. Amberg and J. Ågren, "Phase-Field Simulations of Non-Isothermal Binary Alloy Solidification", *Acta Materialia*, **49**:573 (2001).
- [34] Steinbach, I., F. Pezzolla, B. Nestler, M. Seeßelberg, R. Prieler, G. J. Schmitz and J. L. L. Rezende, "A Phase Field Concept for Multiple Systems", *Physica D*, **94**:135 (1996).
- [35] Tiaden, B. Nestler, H. J. Diepers and I. Steinbach, "The Multiphase-Field Model with an Integrated Concept for Modelling Solute Diffusion", *Physica D*, **115**:73 (1998).
- [36] Venkitachalam, M. K., L. Q. Chen, A. G. Khachaturyan and G. L. Messing, "A Multiple-Component Order Parameter Phase Field Model for Anisotropic Grain Growth", *Materials Science and Engineering*, **A238**:94 (1997).
- [37] Wu, K., J. E. Morral and Y. Wang, "A Phase Field Study of Microstructural Changes due to the Kirkendall Effect in Two-Phase Diffusion Couples", *Acta Materialia*, **49**:3401 (2001).
- [38] Mecozzi, M. G., J. Sietsma, S. van der Zwaag, M. Apel, P. Schaffnit and I. Steinbach, "Analysis of the $\gamma \rightarrow \alpha$ Transformation in a C-Mn Steels by Dilatometry, Laser Scanning Confocal Microscopy and Phase Field Modeling", not yet published (2003).

- [39] Cha, P., S. G. Kim, D. Yeon and J. Yoon, "A Phase Field Model for the Solute Drag on Moving Grain Boundaries", *Acta Materialia*, **50**:3817 (2002).
- [40] Fan, D., L. Chen, and S. P. Chen, "Effect of Grain Boundary Width on Grain Growth in a Diffuse-Interface Field Model", *Materials Science and Engineering*, **A238**:78 (1997).
- [41] Hoyt, J. J., B. Sadigh, M. Asta, and S. M. Fioles, "Kinetic Phase Field Parameters for the Cu-Ni System Derived from Atomistic Computations", *Acta Materialia*, **47**:3181 (1999).
- [42] Martin, J. W. and R. D. Doherty, *Stability of Microstructure in Metallic Systems*, Cambridge University Press, Cambridge, 1976.
- [43] Geiger, J., A. Roósz and P. Barkóczy, "Simulation of Grain Coarsening in Two Dimensions by Cellular-Automation", *Acta Materialia*, **49**:623 (2001).
- [44] Raabe, D., "Introduction of a Scalable Three-Dimensional Cellular Automaton with a Probabilistic Switching Rule for the Discrete Mesoscale Simulation of Recrystallization Phenomena", *Philosophical Magazine A*, **79**:2339 (1999).
- [45] Marx, V., F. R. Reher and G. Gottstein, "Simulation of Primary Recrystallization using a Modified Three-Dimensional Cellular Automation", *Acta Materialia*, **47**:1219 (1999).
- [46] Helfen, L., D. T. Wu, R. Birringer and C. E. Krill III, "The Impact of Stochastic Atomic Jumps on the Kinetics of Curvature-Driven Grain Growth", *Acta Materialia*, **51**:2743 (2003).

- [47] Johnson, W. C., "Effect of Interfacial Kinetic Barriers in Interface Motion in Binary Diffusion Couples", *Metallurgical and Materials Transactions A*, **29A**:2021 (1998).
- [48] Mendeleev, M. I. and D. J. Srolovotz, "Impurity effects on grain boundary migration", *Modelling Simulations in Materials Science and Engineering*, **10**:R79-R109 (2002).
- [49] Gurtin, M.E., "Generalized Ginzburg-Landau and Cahn-Hilliard equations based on a microforce balance", *Physica D* **92**:178–192 (1996).
- [50] Coleman, B.D. and W. Noll, "The thermodynamics of elastic materials with heat conduction and viscosity", *Archive for Rational Mechanics and Analysis*, **13**:245–261 (1963).
- [51] Kuar, I., Y. Mishin, W. Gust, *Fundamentals of Grain and Interphase Boundary Diffusion*, John Wiley, New York (1995).

APPENDICES

A. Appendix: Asymptotic Analysis of the GL Model

A matched asymptotic expansion is performed on the Ginzburg-Landau equations (4.17) to show that, as the non-dimensional parameter, ϵ , tends to zero, the sharp-interface equations (3.13a-3.13c & 3.24a-3.24c) are recovered. The analysis is performed in cylindrical coordinates for both the precipitation code and the grain coarsening code to compare with the axisymmetric sharp interface model. We note that an asymptotic analysis of a much more general system of equations has been performed by Fried and Vendantam [5]. The problem below simply sketches out the analysis required for the present systems being considered.

The analysis proceeds by expanding the governing Ginzburg-Landau equations piecewise between regions far from an interface and at the interface. In each region scalar fields such as ρ , ϕ , and μ , represented by η , are expanded according to powers

of ϵ

($\epsilon < 1$). Let

$$\eta = \eta_0 + \epsilon\eta_1 + \epsilon^2\eta_2 \dots \quad (\text{A.1})$$

Fields expanded in the interfacial region will be differentiated from outer expansion fields by a hat $\hat{\eta}$. The interfacial region can be more smoothly expanded by stretching the scale. This is done by adopting a local coordinate system. If \vec{r} and \vec{s} are coordinate vectors ($\hat{r} \cdot \hat{s} = 0$) and \hat{r} and $\nabla\phi$ are in the same direction then the local radial scale is found from $z = r\epsilon^{-1}$. In this local scale, gradient and laplacian operators are written as

$$\nabla\hat{\phi} = \epsilon^{-1}\hat{r}\frac{\partial\hat{\phi}}{\partial z} + \left(\frac{1}{1+\epsilon z\kappa}\right)\hat{s}\frac{\partial\hat{\phi}}{\partial s} \quad (\text{A.2})$$

$$\begin{aligned} \Delta\hat{\mu} = & \epsilon^{-2}\frac{\partial^2\hat{\mu}}{\partial z^2} + \epsilon^{-1}\left(\frac{\kappa}{1+\epsilon z\kappa}\right)\frac{\partial\hat{\mu}}{\partial z} \\ & -\epsilon\left(\frac{z}{(1+\epsilon z\kappa)^3}\frac{\partial\kappa}{\partial s}\right)\frac{\partial\hat{\mu}}{\partial s} + \left(\frac{1}{(1+\epsilon z\kappa)^2}\right)\frac{\partial^2\hat{\mu}}{\partial s^2} \end{aligned} \quad (\text{A.3})$$

The time derivative of the solute density can also be written in a local, expanded form by realizing $V = -\partial r/\partial t$:

$$\hat{\rho}^\bullet = \frac{\partial\hat{\rho}}{\partial r}\frac{\partial r}{\partial t} = -\frac{V}{\epsilon}\frac{\partial\hat{\rho}_0}{\partial z} + 0(f[\hat{\rho}_1])\epsilon^0 \quad (\text{A.4})$$

Precipitation

The non-dimensionalized Ginzburg-Landau equations for precipitation are

$$\rho^\bullet = M \Delta [\rho - \varphi] \quad (\text{A.5})$$

$$0 = -\epsilon^{-1} f'(\varphi) + \frac{1}{2} - \rho + \gamma \epsilon \Delta \varphi \quad (\text{A.6})$$

Here $\epsilon = K(\rho_m + \rho_p)/f_0$ and $\tilde{\gamma} = k_1 l^2 \epsilon \gamma$.

Outer expansion

For the outer region the higher order terms of ϵ will be neglected leaving the leading order equations

$$\rho_0^\bullet = M \Delta [\rho_0 - \varphi_0] \quad (\text{A.7})$$

$$0 = f'(\varphi_0) \quad (\text{A.8})$$

Applying the exchange energy expression of equation () allows these equations to be reduced to

$$\rho_0^\bullet = M \Delta \rho_0 \quad (\text{A.9})$$

$$\varphi_0 = 0, 1 \quad (\text{A.10})$$

These equations show that away from the interface, the phase order parameter is constant at either a value of 0 or 1.

Inner Expansion

Using the scalar expansion (A.1) and replacing $\hat{\mu} = \hat{\rho} - \hat{\varphi}$, the chemical potential is expanded as

$$\hat{\mu} = (\hat{\rho}_0 - \hat{\varphi}_0) + \epsilon (\hat{\rho}_1 - \hat{\varphi}_1) + \epsilon^2 (\hat{\rho}_2 - \hat{\varphi}_2) + \dots \quad (\text{A.11})$$

The diffusion governing equation is expanded using equation (A.4) and applying the chemical potential to the laplacian expansion (A.3). Likewise the phase field governing equation is expanded and terms scaled by different orders of ϵ are treated as independent. Throwing out all terms but the two highest orders, the relevant expanded governing equations are then

$$\frac{\partial^2 \hat{\mu}_0}{\partial z^2} = 0 \quad (\text{A.12a})$$

$$-V \frac{\partial \hat{\rho}_0}{\partial z} = M\kappa \frac{\partial \hat{\mu}_0}{\partial z} + M \frac{\partial^2 \hat{\mu}_1}{\partial z^2} \quad (\text{A.12b})$$

$$0 = -f'(\hat{\varphi}_0) + \gamma \frac{\partial^2 \hat{\varphi}_0}{\partial z^2} \quad (\text{A.12c})$$

$$0 = -f''(\hat{\varphi}_0)\hat{\varphi}_1 + \frac{1}{2} - \hat{\rho}_0 + \gamma\kappa \frac{\partial \hat{\varphi}_0}{\partial z} + \gamma \frac{\partial^2 \hat{\varphi}_1}{\partial z^2} \quad (\text{A.12d})$$

Boundary conditions must be applied to the chemical potential in the inner region

so as to match up with the outer expansion:

$$\frac{\partial \widehat{\mu}_0}{\partial z} = 0 \quad (\text{A.13})$$

$$\frac{\partial \widehat{\varphi}_0}{\partial z} = \frac{\partial \widehat{\rho}_0}{\partial z} \quad (\text{A.14})$$

To develop a kinetic relation from equations (A.12c, A.12d), we introduce the linear operator

$$L(\widehat{\varphi}_0)[\widehat{\varphi}_1] := -f''(\widehat{\varphi}_0)\widehat{\varphi}_1 + \gamma \frac{\partial^2 \widehat{\varphi}_1}{\partial z^2} = -\frac{1}{2} + \widehat{\rho}_0 - \gamma \kappa \frac{\partial \widehat{\varphi}_0}{\partial z} \quad (\text{A.15})$$

The extreme right-hand side of this expression can be viewed as an eigenvalue of the linear operator, L , with an associated eigenfunction of $\widehat{\varphi}_1$. Likewise,

$$L(\widehat{\varphi}_0)\left[\frac{\partial \widehat{\varphi}_0}{\partial z}\right] = 0$$

by equation (A.12c) so that the eigenvalue for associated with an eigenfunction of $\frac{\partial \widehat{\varphi}_0}{\partial z}$ is 0. The standard orthogonality condition for test functions of a linear operator

(A.15) then implies that

$$\int_{-\infty}^{+\infty} \frac{\partial \widehat{\varphi}_0}{\partial z} \left[-\frac{1}{2} + \widehat{\rho}_0 - \gamma \kappa \frac{\partial \widehat{\varphi}_0}{\partial z} \right] dz = 0 \quad (\text{A.16})$$

This expression can be re-written as

$$\begin{aligned}
\gamma\kappa \int_{-\infty}^{+\infty} \left(\frac{\partial \widehat{\varphi}_0}{\partial z}\right)^2 dz &= -\frac{\widehat{\varphi}_0}{2} \Big|_{-\infty}^{+\infty} + \int_{-\infty}^{+\infty} \widehat{\rho}_0 \frac{\partial \widehat{\rho}_0}{\partial z} dz & (A.17) \\
&= -\frac{\widehat{\varphi}_0}{2} \Big|_{\varphi^-}^{\varphi^+} + \frac{\widehat{\rho}_0^2}{2} \Big|_{\rho^-}^{\rho^+} \\
&= \frac{(\rho^+)^2 + 1 - (\rho^-)^2}{2} = -\rho^+ \\
&= -([\varepsilon] - \mu[\rho])
\end{aligned}$$

Defining the conversion modulus

$$\Gamma := \int_{-\infty}^{+\infty} \left(\frac{\partial \widehat{\varphi}_0}{\partial z}\right)^2 dz, \quad (A.18)$$

carrying out the integration of equation (A.16) with the relationship (A.14), then matching the inner and outer solutions, implies that

$$[\varepsilon] - \dot{\mu}[\rho] = -\sigma\kappa \quad (A.19)$$

where the surface energy, σ , is given by $\sigma = \gamma\Gamma$. Continuity of the chemical potential is guaranteed by equation (A.13), so the remaining sharp-interface equation is obtained is the jump condition associated with mass balance, equation (3.13b). This is accomplished by taking advantage of equation (A.13) to simplify equation (A.12a) and then integrating this latter equation over the entire domain of the transition zone.

Grain Coarsening

For the case of grain coarsening the Ginzburg-Landau equations are

$$0 = M \Delta [(1 + K_n \varphi) \rho] \quad (\text{A.20})$$

$$\varphi^\bullet = -\epsilon^{-1} f'(\varphi) - \frac{1}{2} K_n \rho^2 + \gamma \epsilon \Delta \varphi \quad (\text{A.21})$$

Here $\epsilon = (k_p - k_m) / f_0$ and $\tilde{\gamma} = f_0 l^2 \epsilon^2 \gamma$.

Outer expansion

The leading order equations are now

$$0 = M \Delta [(1 + K_n \varphi_0) \rho_0] \quad (\text{A.22})$$

$$0 = f'(\varphi_0) \quad (\text{A.23})$$

Since the roots of (A.23) are again 0 and 1, and since K_n is a constant, the diffusion equation in the bulk regions reduces to

$$0 = \Delta \rho_0 \quad (\text{A.24})$$

Inner Expansion

In terms of the scalar fields of interest $\hat{\rho}$ and $\hat{\varphi}$, the chemical potential is expanded as

$$\hat{\mu} = (1 + K_n \hat{\varphi}_0) \hat{\rho}_0 + \epsilon(1 + K_n \hat{\varphi}_1) \hat{\rho}_1 + \epsilon^2(1 + K_n \hat{\varphi}_2) \hat{\rho}_2 \dots \quad (\text{A.25})$$

The Ginzburg-Landau equations are expanded, terms of ϵ of order 0 and greater are neglected and the remaining orders of ϵ are balanced:

$$\frac{\partial^2 \hat{\mu}_0}{\partial z^2} = 0 \quad (\text{A.26a})$$

$$0 = M\kappa \frac{\partial \hat{\mu}_0}{\partial z} + M \frac{\partial^2 \hat{\mu}_1}{\partial z^2} \quad (\text{A.26b})$$

$$0 = -f'(\hat{\varphi}_0) + \gamma \frac{\partial^2 \hat{\varphi}_0}{\partial z^2} \quad (\text{A.26c})$$

$$-V \frac{\partial \hat{\varphi}_0}{\partial z} = -f''(\hat{\varphi}_0) \hat{\varphi}_1 - \frac{K_n \hat{\rho}_0^2}{2} + \gamma \kappa \frac{\partial \hat{\varphi}_0}{\partial z} + \gamma \frac{\partial^2 \hat{\varphi}_1}{\partial z^2} \quad (\text{A.26d})$$

Integration of equation (A.26a) and the required boundedness of the chemical potential within the transition zone gives the spacial relationship between the scalar concentration and phase:

$$\frac{\partial \hat{\mu}_0}{\partial z} = 0 \quad (\text{A.27})$$

$$\frac{\partial \hat{\varphi}_0}{\partial z} = -\frac{1}{K_n \hat{\rho}_0} \frac{\partial \hat{\rho}_0}{\partial z} (1 + K_n \hat{\varphi}_0) \quad (\text{A.28})$$

The linear operator found from the kinetic relation from equations (A.26c, A.26d) is

now:

$$L(\widehat{\varphi}_0)[\widehat{\varphi}_1] \quad : \quad = -f''(\widehat{\varphi}_0)\widehat{\varphi}_1 + \gamma \frac{\partial^2 \widehat{\varphi}_1}{\partial z^2} = +\frac{K_n \widehat{\rho}_0^2}{2} - \gamma \kappa \frac{\partial \widehat{\varphi}_0}{\partial z} - V \frac{\partial \widehat{\varphi}_0}{\partial z}. \quad (\text{A.29})$$

$$L(\widehat{\varphi}_0)\left[\frac{\partial \widehat{\varphi}_0}{\partial z}\right] = 0 \quad (\text{A.30})$$

The standard orthogonality condition for test functions of a linear operator then

implies that

$$\int_{-\infty}^{+\infty} \frac{\partial \widehat{\varphi}_0}{\partial z} \left[\frac{K_n \widehat{\rho}_0^2}{2} - \gamma \kappa \frac{\partial \widehat{\varphi}_0}{\partial z} - V \frac{\partial \widehat{\varphi}_0}{\partial z} \right] dz = 0. \quad (\text{A.31})$$

Equation (A.28) implies that

$$\frac{\partial \widehat{\varphi}_0}{\partial z} = \frac{-\rho^+}{K_n \widehat{\rho}_0^2} \frac{\partial \widehat{\rho}_0}{\partial z}$$

so that Equation (A.31) can be re-written as

$$\begin{aligned} (\gamma \kappa + V) \int_{-\infty}^{+\infty} (\partial_z \widehat{\varphi}_0)^2 dz &= \int_{-\infty}^{+\infty} \frac{-\rho^+}{2} \frac{\partial \widehat{\rho}_0}{\partial z} dz \\ &= \frac{-\rho^+ (\rho^+ - \rho^-)}{2} \\ &= \frac{-K_n (1 + K_n) (\rho^-)^2}{2} \\ &= [\varepsilon] - \mu[\rho] \end{aligned}$$

The conversion modulus remains the same

$$\Gamma := \int_{-\infty}^{+\infty} \left(\frac{\partial \widehat{\varphi}_0}{\partial z} \right)^2 dz.$$

The above expressions therefore imply that

$$\Gamma V = [\varepsilon] - \mu[\rho] - \sigma\kappa \tag{A.32}$$

This is the kinetic equation presented in the sharp-interface theory provided that the $M = 1/\Gamma$. Continuity of the chemical potential is guaranteed by equation (A.13), so the remaining sharp-interface equation to obtain is the jump condition associated with mass balance, equation (3.24b). This is accomplished by taking advantage of equation (A.13) to simplify equation (A.26a) and then integrating this latter equation over the entire domain of the transition zone.

B. Appendix: Parabolic Approximation of Free Energy Curve

In developing the theory behind grain boundary migration we approximated a Gibbs free energy curve for a binary system as a parabolic function of concentration. If this is the approximation, what is the actual form of the free energy and is this approximation justified? The argument begins with the contribution of the molar quantity of each species to the Gibbs free energy in an unmixed system [1].

$$G_{unmixed} = X_A G_A + X_B G_B \quad (\text{B.33})$$

The reduction in free energy due to mixing of two species is reflected in the entropy and enthalpy changes.

$$\Delta G_{mix} = \Delta H_{mix} - T \Delta S_{mix} \quad (\text{B.34})$$

For an ideal solution the enthalpy does not change ($\Delta H_{mix} = 0$) and ΔS_{mix} is found through statistical mechanics to be

$$\Delta S_{mix} = -R(X_A \ln X_A + X_B \ln X_B). \quad (\text{B.35})$$

$$G = X_A G_A + X_B G_B + R(X_A \ln X_A + X_B \ln X_B) \quad (\text{B.36})$$

Including equation (B.35) in (B.34) and adding to $G_{unmixed}$ gives the free energy of equation (B.36). This then is the correct form that needs to be compared to equation (2.8). Algebraically combining these two equations leads to a transcendental function. Figure 7.1 shows actual form of the free energy, a parabolic function numerically fit to this curve and the difference between the two. The choice of $G = 0$ is arbitrary and the error is independent of this choice. As the error is zero at the minimum of the curves and grows only as the Gibbs becomes large in comparison, the approximation is satisfying at all concentrations. Indeed, we are only concerned with processes that have reached equilibrium and hug G_{\min} .

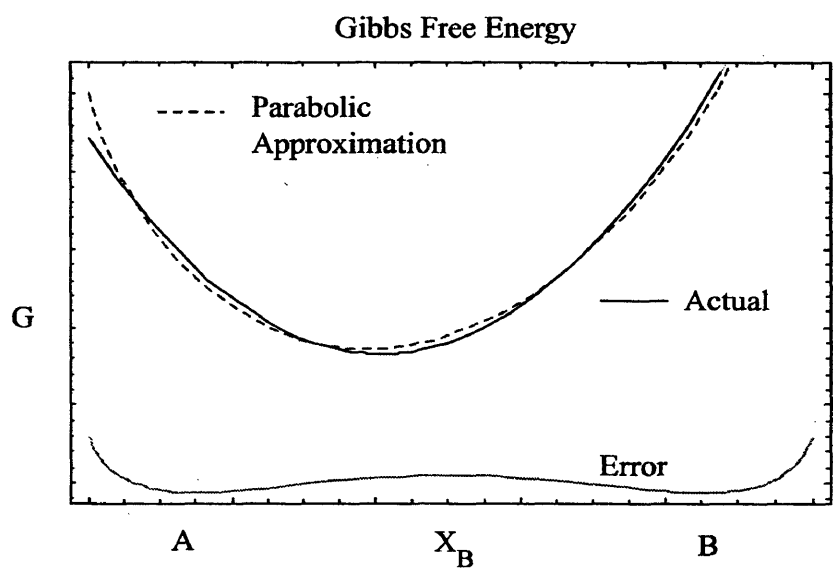


Figure 7.1: Comparison of Gibbs free energy of the form of eqn. B.36, a parabolic function fit to eqn B.36 and the error associated with the fit function.